JGR Space Physics

RESEARCH ARTICLE
10.1029/2024JA032999

Influence of Lower Atmospheric Variability: An Investigation of Delayed Ionospheric Response to Solar Activity

Rajesh Vaishnav[1], Christoph Jacobi[1], Erik Schmölter[2], and Hanna Dühnen[2]

[1]Leipzig Institute for Meteorology, Leipzig University, Leipzig, Germany, [2]German Aerospace Center, Neustrelitz, Germany

Key Points:

- The variations in thermospheric-ionospheric parameters caused by tidal forcing have been examined using TIEGCM simulations
- Lower atmospheric forcing influences the ionospheric delay during low solar activity
- At the 27-day time scale, the ionospheric delay in electron density against solar flux variations is about 19 hr

Correspondence to:

R. Vaishnav,
rajesh_ishwardas.vaishnav@uni-leipzig.de

Citation:

Vaishnav, R., Jacobi, C., Schmölter, E., & Dühnen, H. (2024). Influence of lower atmospheric variability: An investigation of delayed ionospheric response to solar activity. *Journal of Geophysical Research: Space Physics*, *129*, e2024JA032999. https://doi.org/10.1029/2024JA032999

Received 25 JUN 2024
Accepted 12 NOV 2024

Abstract This study aims to examine the impact of lower atmospheric forcing on upper atmospheric variability using the Thermosphere-Ionosphere-Electrodynamics General Circulation Model (TIEGCM). We conducted numerical experiments comparing induced variability due to Hough Mode Extension (HME) tides constrained by winds and temperatures from Ionospheric Connection Explorer-Michelson Interferometer for Global High-Resolution Thermospheric Imaging (ICON-MIGHTI) observations. Our model comparisons focus on the changes in the composition of the thermosphere-ionosphere and the delayed ionospheric response to the 27-day solar EUV flux variations during periods of low solar activity. We report the results of model simulations with and without tidal forcing at the approximate 97 km lower boundary of the TIEGCM. The differences led to changes in thermosphere-ionosphere parameters such as electron density, peak electron density, and the O/N_2 ratio. The results show that the impact of tidal forcing is mainly observed in the low- and mid-latitude regions, affecting the correlation between O/N_2 and NmF2. This change in correlation affects the amount of ionospheric delay. When tidal forcing is included, the modeled delay improves compared to the observed delay during low solar activity. The spatial variation of ionospheric delay due to induced tidal effects highlights the importance of understanding lower atmospheric forcing in thermosphere-ionosphere models. This is crucial for predicting and understanding the ionospheric response to solar flux.

1. Introduction

The thermosphere-ionosphere (TI) is a highly complex dynamical system controlled not only by extreme ultraviolet (EUV) and ultraviolet (UV) radiation from the Sun and geomagnetic perturbations, but also by conditions in the lower atmosphere (Rishbeth & Mendillo, 2001). Recent studies show that forcing from below (tropospheric and stratospheric sources) play an important role in the behavior of the ionosphere (Knížová et al., 2021; Liu, 2016; Oberheide et al., 2015; Yiğit & Medvedev, 2015). The TI variability is driven by atmospheric tides, planetary waves, and gravity waves. Understanding the changes in the behavior of the ionosphere triggered by various factors, such as chemical and thermal influences, requires knowledge of the different forcing mechanisms. Using model experiments and observations, several studies have reported the relative contribution of different forcing, such as solar, lower atmosphere, and geomagnetic forcing, to the global ionosphere variability (Fang et al., 2013; Forbes et al., 2000; Rishbeth & Mendillo, 2001). Among all the forcing, lower atmospheric forcing contribute approximately 15%–35% of the variability in the ionospheric F2-layer electron density (NmF2) (Forbes et al., 2000).

The recent advancements in modeling the TI have led to the creation of detailed numerical models. These models can incorporate daily changes in lower and middle atmospheric wave activity using observational or reanalysis data through nudging techniques and data assimilation. For example, using a global ionosphere-plasmasphere model with electrodynamics driven by a Whole Atmosphere Model (WAM) simulation, Fang et al. (2013) have shown that perturbations from the lower atmosphere account for about half of the observed variability in NmF2 under moderate solar activity and geomagnetically quiet conditions. Furthermore, the influence of lower atmospheric perturbations on the ionospheric variability also depend on the solar activity (Liu et al., 2010, 2013; Zhou et al., 2020, 2021).

Several authors have reported the role of lower atmospheric forcing in the ionosphere during sudden stratospheric warming (SSW: Chau et al., 2012; Goncharenko & Zhang, 2008; Kazimirovsky & Kokourov, 1991). For example, Goncharenko and Zhang (2008) investigated the lower atmosphere-ionosphere coupling during SSWs

and reported that the observed cooling and warming in the ion temperature is associated with stratospheric warming. This association may be attributed to the notion that significant alterations in atmospheric parameters are more readily induced at higher altitudes due to lower neutral density.

Pedatella et al. (2016) and Jones et al. (2018) used different whole atmosphere models to highlight the variability of the TI with different lower atmospheric backgrounds during SSW and demonstrated that different nudging techniques influence model results. Siskind et al. (2014) used a set of NCAR Thermosphere-Ionosphere-Electrodynamics general circulation model (TIEGCM: Richmond et al. (1992)) simulations with different tidal forcing and demonstrated that the vertical transport by nonmigrating tides causes a significant reduction in NmF2. The observed effect is attributed to the augmented downward transport of atomic oxygen to the base of the thermosphere, leading to a greater relative abundance of N_2 and, consequently, an enhanced recombination of ions and electrons. Additionally, various mechanisms may contribute to changes in TI composition due to tidal forcing. This could be attributed to transport processes (Jones et al., 2018), mean meridional circulation (Yamazaki & Richmond, 2013), and three-body recombination processes (Forbes et al., 1993). Vaishnav, Jacobi, et al. (2021) examined the role of vertical transport processes in the TI system and highlighted their significance in the ionospheric composition changes using the Coupled Thermosphere Ionosphere Plasmasphere electrodynamics (CTIPe: Codrescu et al., 2012) model.

In a recent study by Forbes et al. (2024), the day-to-day variability associated with the TI parameters due to forcing from below (tidal forced run) and forcing from above (solar and geomagnetic forcing) was investigated using TIEGCM simulations. They found that lower atmospheric forcing, such as tides, as well as solar and geomagnetic forcing play a significant role in this variability via processes such as vertical transport, photoionization, adiabatic heating and cooling. In the case of the tidal forced run, the dissipation of the vertically propagating tidal spectrum leads to temperature increases and larger scale heights. This often occurs alongside downwelling and is likely due to subsidence heating. The resulting decreases in O/N_2 at altitudes above 150 km are consistent with the hydrostatic law and corresponding temperature increases, explaining reductions of up to 30%–40% in electron density (Ne) in the F-region. However, in contrast, in the case of a solar and geomagnetic forcing run, these O/N_2 depressions are not sufficient to reduce electron densities. Instead, Ne actually increases due to solar production associated with the elevated solar fluxes, which overcompensates for the O/N_2 effect.

The 27-day solar rotation period is a well-studied solar flux variation mode. This radiation mode is significantly enhanced and amplified during high solar activity, resulting in modulation in the TI system (Kutiev et al., 2013; Min et al., 2009). However, the ionospheric Ne reacts to this solar variation with a time delay of about 18 hr to 2 days (so called delayed ionospheric response). The relationship between the TI parameters such as NmF2, total electron content (TEC), temperature, neutral densities and 27-day solar EUV flux variations has been extensively studied by various authors (e.g., Afraimovich et al., 2008; Jacobi et al., 2016; Jakowski et al., 1991; Ren et al., 2018, 2020; Schmölter et al., 2018, 2022, 2024; Vaishnav et al., 2018, 2019). The impact of geomagnetic activity on the ionospheric delay has also been studied (Schmölter et al., 2020), which was later demonstrated by the model simulations (Vaishnav, Schmölter, et al., 2021). In a recent study, Schmölter et al. (2024) examined the delayed ionospheric response to solar activity during both low and high solar activity. They found that ionospheric delay increases toward mid-latitudes, especially at the equatorial ionization anomaly during periods of high solar activity.

In addition to solar and geomagnetic activity, transport processes are reported to be an important parameter affecting the ionospheric delay mechanism, with an increase of transport leading to a decrease in delay (Vaishnav, Schmölter, et al., 2021). Recent studies have reported that the ionospheric delay could be related to the response time of O/N_2 (Ren et al., 2018; Schmölter et al., 2021; Vaishnav, Jacobi, et al., 2021). Furthermore, the spatio-temporal and altitudinal dependence of the ionospheric delay have been reported by Schmölter et al. (2022) and Vaishnav et al. (2022). Vaishnav et al. (2024) found a positive correlation between O/N_2 and solar flux at mid-latitudes (25°N-55°N) during the low solar activity period. However, for other latitudes, a negative correlation indicates the possible influence of other factors, such as geomagnetic activity and lower atmospheric forcing, which affect the O/N_2 ratio, especially during low solar activity. The role of solar and geomagnetic activity has been discussed with observations and model simulations (Ren et al., 2018; Schmölter et al., 2021; Vaishnav, Jacobi, et al., 2021), and it is crucial to comprehend the role of lower atmospheric forcing using numerical modeling. Recently, Maute et al. (2023) used TIEGCM simulations to examine the impact of tidal forcing on the

TI composition. They showed a 15%–20% change in the zonal and diurnal mean NmF2 with a roughly 10% modification in the O/N_2 ratio from 7 August to 26 September 2020, associated with strong tidal variation.

By comparing model simulations with and without tidal forcing, it is possible to isolate and quantify the effects of lower atmospheric forcing on the TI system variability. This also helps us to understand the influence of solar flux variations on the delayed ionospheric response in the TI system, and compare the consequences of tidal forcing on O, O_2 in the thermosphere and Ne in the ionosphere. The presented modeling results then will show how lower atmospheric forcing affects ionospheric delay and highlight limitations in the physics-based numerical model, necessary for further atmospheric modeling improvements.

The manuscript is organized as follows. Section 2 provides an introduction to the data sources and the TIEGCM model. In Section 3, we present the results of our investigations of the influence of tides on various TI parameters, as well as the delayed ionospheric response to solar EUV variations. Section 4 discusses our findings and concludes the paper.

2. Observations and Model

To analyze ionospheric variability, global ionospheric TEC maps from the International GNSS Service (IGS) provided by NASA's Data Archive Service are used (NASA, 2024a; Noll, 2010). We used 2-hourly global TEC maps available at a spatial resolution of 2.5°/5° in latitude and longitude. The F10.7 index is a widely used measure of solar activity, and we utilize daily F10.7 values available from the LISIRD database (LASP, 2024a). The Solar EUV Monitor (SEM, Judge et al., 1998) aboard the Solar Heliospheric Observatory (SOHO) has been monitoring solar EUV fluxes in the 26–34 nm and 0.1–50 nm wavebands since 1996. In this study, we utilized the central-order flux at 1 AU (0.1–50 nm) with hourly resolution. The SOHO/SEM EUV fluxes (hereafter EUV) are available from the LISIRD database (LASP, 2024b).

The SES-14 communications satellite is equipped with the Global-scale Observations of the Limb and Disk (GOLD) instrument (Eastes et al., 2017, 2020). Its primary function is to measure Earth's airglow emissions from 134 to 162 nm during the day and O 135.6 nm emissions at night (Correira et al., 2021). To retrieve the column density ratio O/N_2, GOLD uses an algorithm that was previously used with the Global Ultraviolet Imager (GUVI) and the Special Sensor Ultraviolet Spectrographic Imager (SSUSI). However, GOLD's algorithm takes advantage of transmitting the full spectrum to maximize the signal-to-noise ratio (NASA, 2024b). This study used GOLD's version 4 data.

We have utilized TIEGCM simulations (version 2.0) to analyze the impact of lower atmospheric forcing on the neutral composition and to investigate its role in the ionospheric delay mechanism. The TIEGCM is a global 3-D, numerical, and physics-based thermosphere ionosphere electrodynamics model that efficiently solves the Eulerian continuity, momentum, and energy equations (Qian et al., 2014; Richmond & Maute, 2014). For this study, the model is run with a horizontal resolution of $2.5^\circ \times 2.5^\circ$ in longitude and latitude, and with a vertical resolution of a quarter of the scale height. The altitude is determined based on the pressure surfaces, which are defined as pressure levels = ln(P0/P), where P0 is a reference pressure of 5×10^{-7} hPa, and pressure levels range from −7 (altitude ≈97 km) to 7 (≈500 km), depending on solar activity. External inputs such as solar, geomagnetic, and lower atmospheric forcing are used to drive the model. For solar input, the model incorporates a reference solar spectrum based on the EUV flux model for Aeronomic Calculations (EUVAC) (Richards et al., 1994) driven by variations of F10.7, its 81-day average and a set of wavelength-dependent ionizations rates. For the polar region, the model employs inputs from high-latitude convection and aurora models. The magnetosphere-ionosphere coupling is simulated by specifying the ion convection pattern given by Weimer (2005). The auroral precipitation is based on the analytical model developed by Roble and Ridley (1987) with parametrization provided by Emery et al. (2012). Moreover, the model uses a specified lower boundary at a constant pressure level, around 97 km.

Additionally, to investigate the impact of tidal forcing, TIEGCM may incorporate the Ionospheric Connection Explorer (ICON) observations, as described by Maute (2017). At the lower boundary (97 km) of the model, the tidal fitting obtained from the ICON-Michelson Interferometer for Global High-Resolution Thermospheric Imaging (ICON-MIGHTI) observations is utilized after being fitted to Hough Mode Extensions (HME) (Cullens et al., 2020; Forbes et al., 2017). This product characterizes the zonal wind, meridional wind, temperature, and geopotential height perturbations caused by diurnal and semidiurnal tides based on ICON-MIGHTI observations

from 94 to 102 km within the latitude range of 10°S-40°N over a 35-day window (Cullens et al., 2020). The simulations that incorporate the HME product will be referred to as TIEGCM-HME. The detailed HME methodologies are described in Forbes et al. (1994) and Oberheide et al. (2011). HME for ICON and application to TIEGCM simulations is summarized in Forbes et al. (2017) and Maute (2017), respectively, and sensitivity studies of HME fitting to the data coverage can be found in Cullens et al. (2020). Cullens et al. (2020) showed that the HME-forced TIEGCM represents the lower thermosphere similar to a fully simulated model with input from the middle atmosphere.

In this study, we aim to investigate the impact of upward propagating tides on the ionospheric delay during two specific time periods: from 26 July to 21 August 2020 and from 8 July to 3 August 2021. We selected the study period based on the availability of an observed 27-day solar rotation period, low solar activity (F10.7 $<$ 100 sfu), and low geomagnetic activity (Kp index $\leq$ 3). Observing the 27-day solar rotation period during low solar activity is crucial. Therefore, we precisely chose the period from 26 July to 21 August 2020, when solar activity is low. This period is suitable for investigating the impact of lower atmospheric forcing and observing the solar rotation period. We also selected a second period from 8 July to 3 August 2021 based on the same criteria but with slightly higher solar activity. This will be suitable for investigating the impact of solar activity and ionospheric delayed response. After this second period, solar activity continuously increases, dominating the lower atmospheric forcing. Due to the limited number of solar rotation periods, we carefully chose these two periods. We will utilize the ICON-TIEGCM level 4 data products (v01r000 for TIEGCM and v02r000 for TIEGCM-HME runs) for our analysis.

3. Results

In this section, we will discuss the impact of lower atmospheric forcing on the TI composition during the study period and its effect on the ionospheric delay. Recently, Vaishnav et al. (2024) highlighted the possible impact of lower atmospheric forcing on ionospheric delay. To further investigate this, we use the TIEGCM simulation to examine the effects of lower atmospheric forcing on the ionosphere. Results of the following model runs will be analysed to showcase this effect.

1. TIEGCM Run: The model was run with the default setting and without tides at the lower boundary.
2. TIEGCM-HME Run: The model was run with the default setting and additionally driven by tides fitted to ICON observations via the HME method.

3.1. Solar and Geomagnetic Activity Variations

Figure 1a shows solar and geomagnetic activity from 21 July to 26 August 2020. The study period corresponds to a solar rotation period, marked by dashed lines (period 1: 26 July to 21 August 2020). The solar activity peaked at around 77 sfu and dropped to a minimum of 72 sfu. The geomagnetic activity was considerably moderate ($Kp = 3$) during the rising part of this solar cycle, which may be considered as a geomagnetically unsettled or moderately disturbed period. It is worth noting that geomagnetic activity plays a crucial role in influencing the ionospheric composition, even during quiet geomagnetic periods, as pointed out by Qian et al. (2022). Nonetheless, our study primarily focuses on the lower atmospheric forcing. During this period, the variation in solar flux is approximately 4 sfu, and solar activity is notably low. Therefore, this period would be suitable for investigating the influence of lower atmospheric forcing. However, it may be challenging to calculate the ionospheric delay during this time. As a result, we opted to also utilize the second study period from 8 July to 3 August 2021 (period 2), as depicted in Figure 1b. Despite the continued low solar activity, the observed solar rotation period is quite favorable, and the variation between minimum and maximum of the F10.7 index is approximately 23 sfu. This circumstance will likely facilitate a more accurate calculation of the delay compared to period 1. Geomagnetic activity is moderate throughout this period, with maximum activity observed on 28 July.

The lower panels of Figure 1 display the observed daily mean TEC for a fixed local time (12:00) as a function of latitude and time at 0°E. TEC is a useful indicator of changes in the ionospheric conditions, and it can vary due to a variety of factors, including solar and geomagnetic activity. During the study period 1, the TEC levels ranged from a minimum of 2 TECU at high latitudes in Southern Hemisphere (SH) to a maximum of 14 TECU near the equator, reflecting the generally low electron densities during low solar activity (Figure 1c). The ionosphere, due to its low electron density during period 1, is highly sensitive to variations in solar and geomagnetic activity. Even minor disturbances can lead to significant changes, which is why geomagnetic activity has a notable impact, even

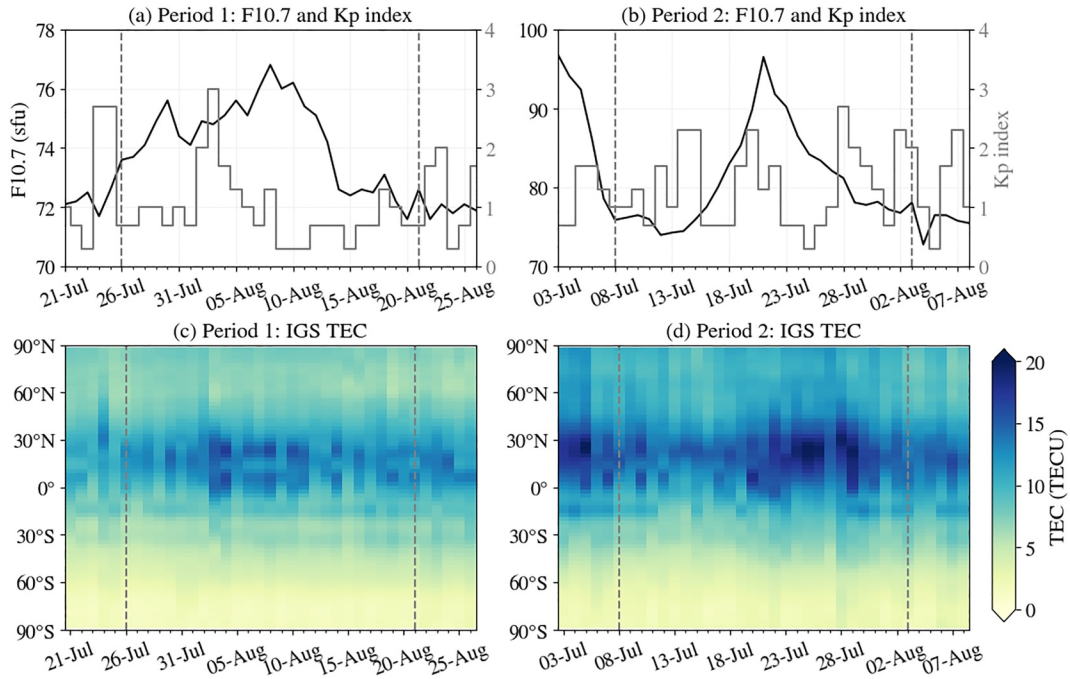

Figure 1. Upper panels: Variations in F10.7 and Kp index from 21 July to 26 August 2020 (a) and from 3 July to 8 August 2021 (b). Lower panels: Corresponding daily mean IGS TEC at 0°E (c, d). The selected study periods are indicated by the dashed lines: period 1 (from 26 July to 21 August 2020) (a) and period 2 (from 8 July to 3 August 2021) (b).

when the Kp index is only up to 3. On 3 and 4 August, the maximum TEC of approximately 14 TECU was observed at low latitudes, which has been influenced by slightly enhanced geomagnetic activity observed on 3 August. On 8 August 2020, the second maximum TEC of approximately 12 TECU was observed in the low-latitude region, associated with the peak of solar activity. Compared to period 1, there is an observed increase in solar activity and moderate disturbance in geomagnetic activity throughout period 2, as reflected in the TEC depicted in Figure 1d. The TEC exhibits a notable peak reaching approximately 20 TECU from day 14 (21 July) to day 22 (29 July), displaying considerable variability and not showing a strict correlation with solar activity post-peak. This period seems to be highly influenced by geomagnetic activity, leading to substantial TEC variability.

In the next section we discuss the impact of lower atmospheric forcing in the TI system and its role in the ionospheric delay.

3.2. Variations in TI Parameters

The zonal wind (Un) characteristics for TIEGCM-HME at 0°N geographic latitude and an altitude of 100 km (lower boundary) at 12:00 UT during period 1 and period 2 are depicted in Figures 2a and 2c, respectively, as a function of time and longitude. Figures 2b and 2d show the difference between TIEGCM-HME and TIEGCM simulated zonal wind during period 1 and period 2, respectively. The difference plots show the effect of the HME tidal forcing applied at the lower boundary of the TIEGCM. In both study periods, we can clearly see the presence of the higher wavenumber 3, as indicated by the gray circles in Figures 2b and 2d. To further explore the influence of the lower atmospheric forcing on the upper atmosphere, we also examine the zonal wind at 250 km. Similar to the upper panel, Figures 2e–2h shows the zonal wind at 250 km for both periods 1 and 2. Again, the difference plot mostly filters out the in situ diurnal tides resulting from the absorption of solar radiation in the F-region, allowing for a clearer visualization of the impact of HME tides (Figures 2f and 2h). However, it is important to note that some minor effects of geomagnetic activity are still present in the difference plot, even though the difference removes the geomagnetic effect (Figure 2b). The zonal wind clearly shows a wavenumber 1 variability in Figure 2e. However, higher wavenumbers are visible in the difference plots, as indicated by the gray circle (Figures 2f and 2h). The difference plot suggests that higher-order wavenumbers are distinctly observable till 23

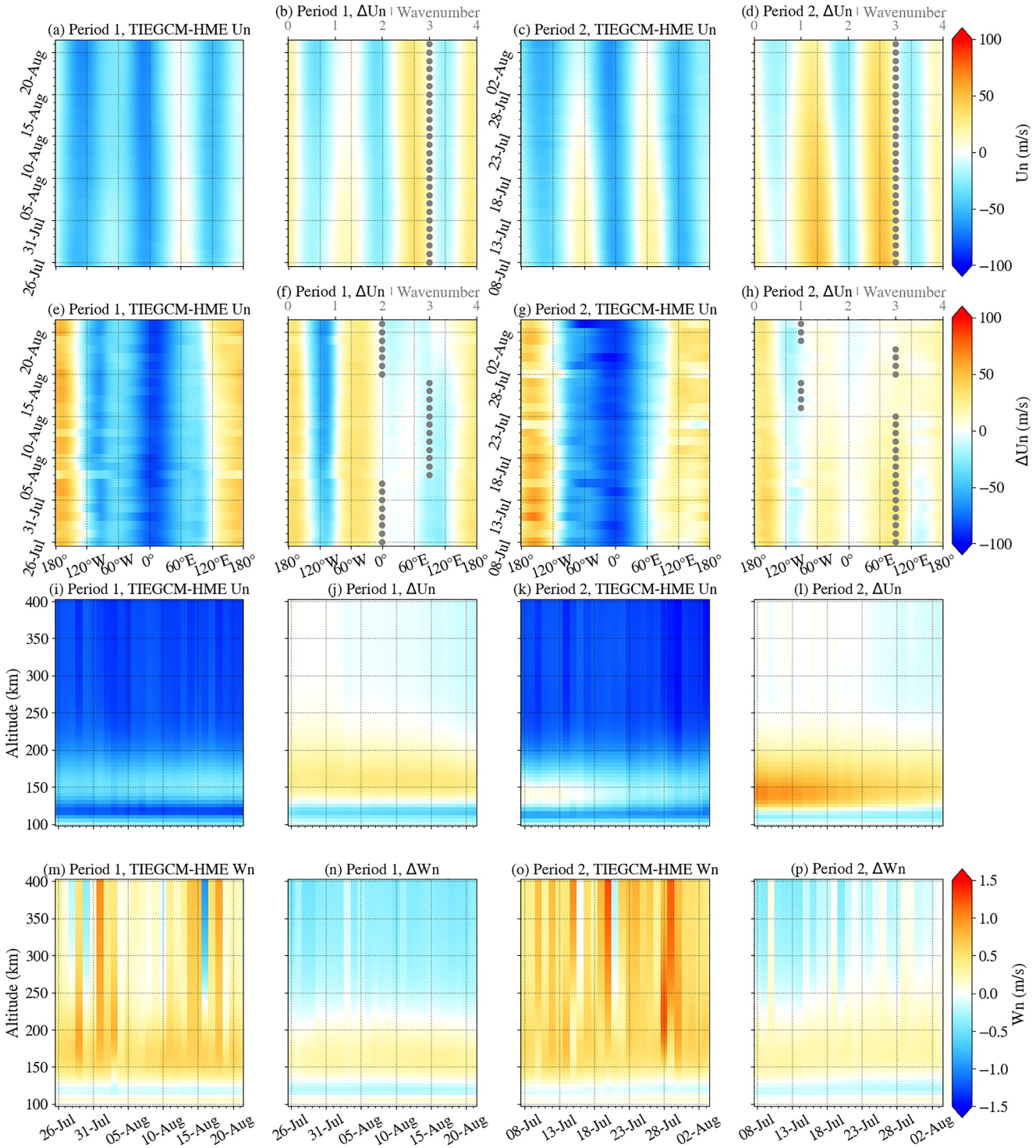

Figure 2. The upper panels (a–d) and middle panels (e–h) display the zonal wind (Un) at 100 and 250 km, respectively, and 0°N at 12:00 UT. The middle panels (i–l) shows the zonal wind, and the lower panels (m–p) display the vertical wind (Wn) at 0°N, 0°E. Each panel contains data from TIEGCM-HME, and the difference between TIEGCM-HME and TIEGCM. The left panels (a, e, i, m) represent period 1, the middle panels (b, f, j, n) illustrate the difference during period 1, the panels (c, g, k, o) represent period 2 and the right panels (d, h, l, p) depict the difference during period 2. In the upper and middle panels (b, d, f, h), the top *x*-axis shows the wavenumber. The gray circles in (b), (d), (f), and (h) show the dominant wavenumber.

July during period 2 (Figure 2h), while wavenumbers 2 and 3 are observed during period 1 (Figure 2f). The difference plots with positive differences indicating stronger (more easterly) winds in TIEGCM-HME.

Figures 2i and 2k in the middle panel displays the zonal wind plotted against altitude and time at 0°N, 0°E during periods 1 and 2, respectively. Figures 2j and 2l illustrate the difference between the TIEGCM-HME and TIEGCM simulated zonal wind for period 1 and period 2, respectively. The largest changes in zonal wind of approximately 10–15 m/s occur between 130 and 200 km. In comparison to the difference plot for period 1, the plot for period 2 depicts stronger easterly winds with a magnitude of about 20–60 m/s.

The lower panels demonstrate the characteristics of the vertical wind (Wn). In Figures 2m–2p, the variations in vertical wind for TIEGCM-HME, along with the difference plots between TIEGCM-HME and TIEGCM, are shown for both period 1 (Figure 2n) and period 2 (Figure 2p). During period 1, there is an observed overall decrease in vertical wind of approximately 10–30 cm/s between 120 and 135 km, and an increase of about 10–50 cm/s between 135 and 210 km (Figure 2n). The decrease in WN on 3 August is caused by an increase in geomagnetic activity. Upon comparing Figures 2n–2p, it is noted that they exhibit similar characteristics during period 2. The vertical wind decreases to about 20–40 cm/s between 120 and 150 km, while it increases to about 30–40 cm/s between 120 and 230 km. These differences suggest that the vertical wind's variations occur from day to day.

Figure 3 illustrates the variation of daily mean mass mixing ratio (mmr) of atomic oxygen (O), molecular oxygen (O_2), molecular nitrogen (N_2), and daily mean atomic oxygen ions (O^+) as a function of altitude and day during period 1 for the TIEGCM run at 0°N, 0°E. Here, mmr(N_2) is calculated by 1—mmr(O)— mmr(O_2). Due to very low solar activity, the daily fluctuations in atomic and molecular oxygen are minimal. Atomic oxygen increases with altitude as shown in Figure 3a, while maximum molecular oxygen is observed in the lower thermosphere below 150 km and decreases with altitude (Figure 3b). Similar to molecular oxygen, molecular nitrogen is also observed to decrease with altitude, with a higher mixing ratio observed in the lower altitudes (Figure 3c). Figure 3d shows the density of atomic oxygen ions, with the maximum ion density observed between 300 and 350 km altitude range, peaking on 8 August following the solar activity peak as depicted in Figure 1a. The minimum ion density is observed on 3 and 4 August. The decrease in ion density can be attributed to geomagnetic activity.

The lower panels of Figure 3 display the percentage difference ((TIEGCM-HME—TIEGCM)/TIEGCM) between TIEGCM and TIEGCM-HME simulated O, O_2, N_2, and O^+ at 0°N, 0°E. Figure 3e shows that with tidal forcing above 110 km the atomic oxygen density decreases by about 2%–4% throughout the study period as compared to the run without tidal forcing. During period 1, solar activity is very low. As a result, lower atmospheric forcing dominates over solar forcing. The increased mixing leads to a decrease in atomic oxygen at higher altitudes. With tidal forcing, molecular oxygen increases with altitude above 110 km by about 2%–6%, as shown in Figure 3f. Similar trends are observed in molecular nitrogen, with an increase of about 1%–3% below 200 km and 3%–7% above 200 km (Figure 3g). In Figure 3h, we present a comparison between the simulated atomic oxygen ion density of TIEGCM and TIEGCM-HME, highlighting the percentage difference. The figure illustrates that the ion density decreases by up to 17% above 230 km. However, in the altitude range of 115–145 km, the ion density increases by about 10%–15%.

This shows that increasing tidal activity modifies the composition by altering the loss of O_2 through photodissociation and O recombination. This results in an increase in molecular oxygen and molecular nitrogen, which leads to a decrease in atomic oxygen at all altitudes above 100 km due to molecular diffusion. As a result, the overall O/O_2 and O/N_2 ratios decrease, which is consistent with previous findings that used the eddy diffusion coefficients (Qian et al., 2009; Rees & Fuller-Rowell, 1988; Vaishnav, Jacobi, et al., 2021). The decrease in atomic oxygen leads to a reduction in the atomic oxygen ion density due to less availability of atoms for ionization processes. This, in turn, impacts the balance between ionization and recombination, resulting in an overall decrease in ion density.

In a similar manner to Figures 3 and 4 illustrates the variations in daily mean atomic oxygen, molecular oxygen, molecular nitrogen, and atomic oxygen ions during period 2, which experienced slightly high solar activity compared to period 1. The daily variations due to solar and geomagnetic activity are visible. The lower row shows the corresponding differences between the TIEGCM and TIEGCM-HME simulated parameters. Figure 4e shows that the overall atomic oxygen density increased by about 3%–7% above 110 km throughout the study period. In

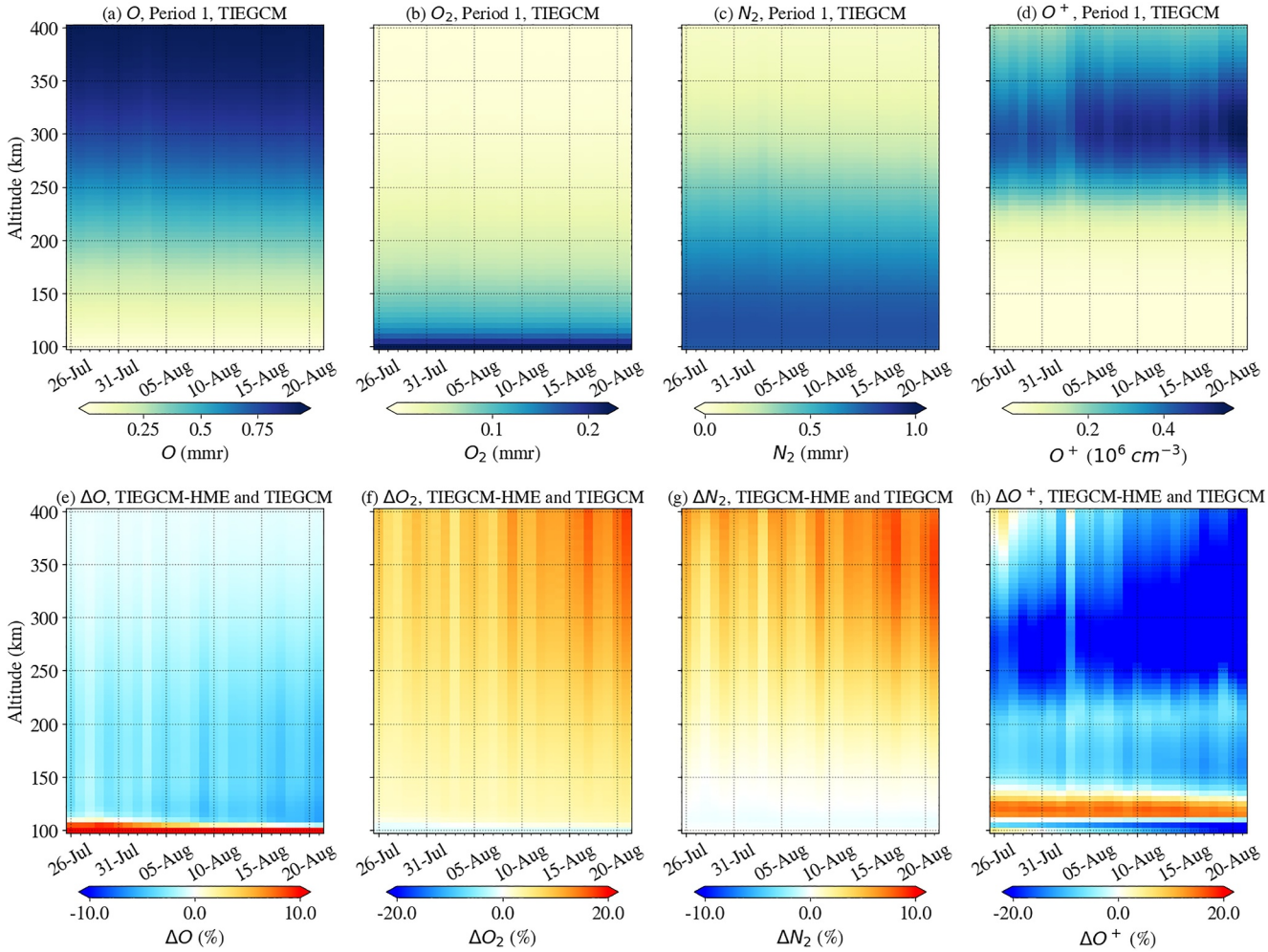

Figure 3. The variations in daily mean (a) atomic oxygen (O), (b) molecular oxygen (O_2), (c) molecular nitrogen (N_2), and (d) atomic oxygen ions (O^+) simulated from TIEGCM as a function of altitude and day for period 1 (26 July–21 August 2020) at 0°N, 0°E. The lower panels demonstrate the corresponding percentage differences between TIEGCM-HME and TIEGCM (e–h).

comparison to atomic oxygen, molecular oxygen behaved oppositely as shown in Figure 4f. Figure 4h shows the percentage difference in atomic oxygen ion density. The ion density increases by about 9%–15% between 120 and 145 km, by about 3%–5% between 200 and 230 km, and by about 5%–15% also above 350 km. Overall, there is an increase in atomic oxygen ion density during this time period. In comparison to period 1, during period 2, the ionization increases with tidal input. However, this suggests the role of transport processes. Figures 3 and 4 indicate the strongest difference between periods 1 and 2 exists in the topside ionosphere.

Figures 5a and 5d shows the variations in diurnal averaged Ne at 0°N, 0°E using TIEGCM during periods 1 and 2 as a function of altitude and day, while its percentage difference with TIEGCM-HME (Figures 5b and 5e). The grey curve represents the F10.7 index (Figures 5a and 5d) and Kp index (Figures 5b and 5e). Figure 5a indicates that due to low solar activity, there was less variation in Ne. However, Ne still displayed small fluctuations correlated to solar activity. As previously reported, during low solar activity, other external factors such as lower atmospheric forcing and geomagnetic activity become more dominant and cause changes in Ne. Figure 5b shows the percentage difference between TIEGCM-HME and TIEGCM ((TIEGCM-HME—TIEGCM)/TIEGCM), with blue colors indicating higher Ne in TIEGCM than in TIEGCM-HME. During period 1, there was a decrease of about 15%–20% in Ne above 250 km. While less decrease observed in below 250 km about 1%–3%. On 3 August 2021, there was a slight less decrease to about 5%, which may be attributed to geomagnetic activity. Despite efforts to remove the geomagnetic effect, some of its effects still remain. However, a difference can be observed between the Ne simulated by TIEGCM and TIEGCM-HME. Above about 140 km TIEGCM-HME with tidally

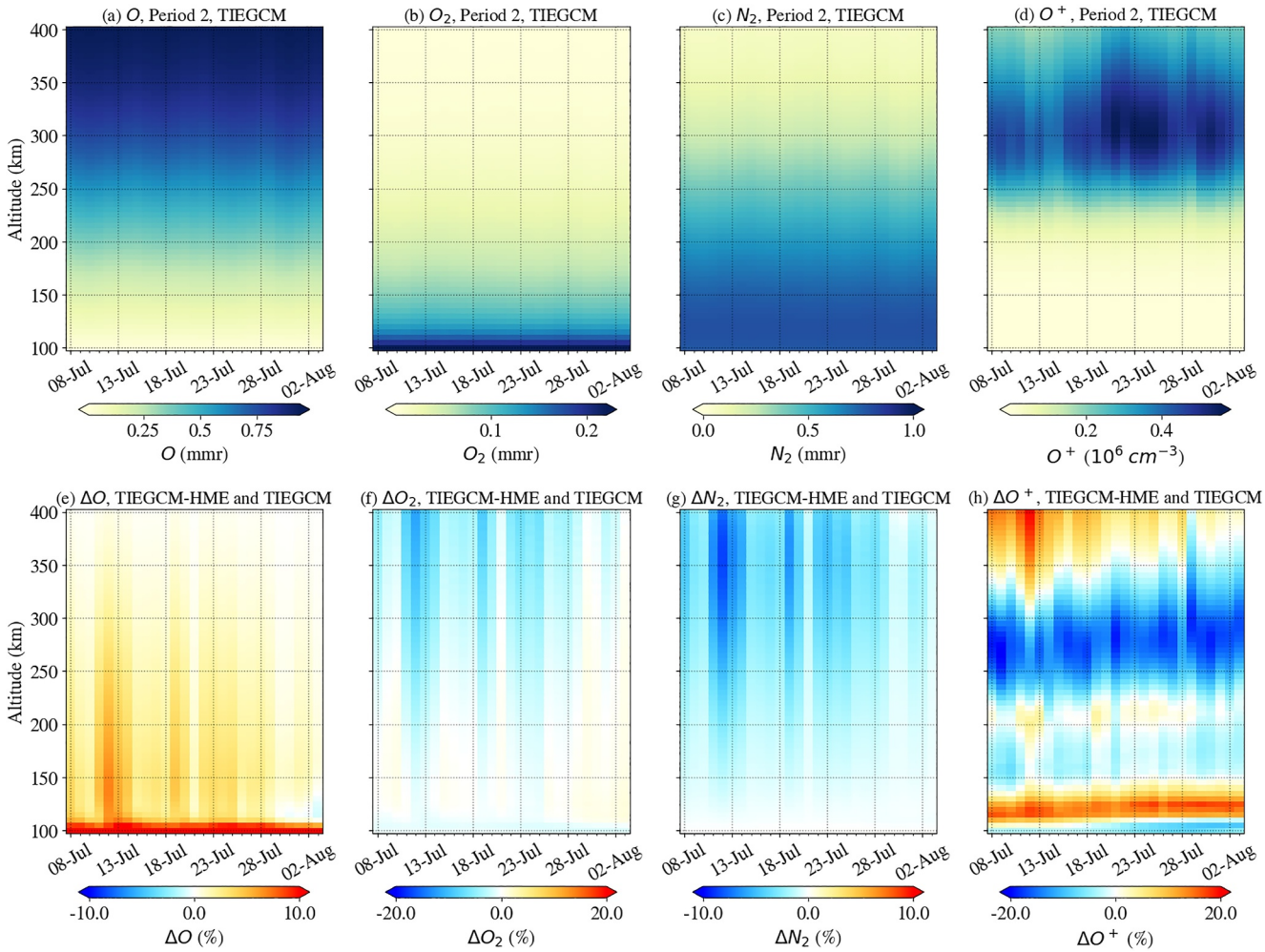

Figure 4. Same as shown in Figure 3, but for period 2 (8 July to 3 August 2021).

forced simulation shows lower Ne as compared to TIEGCM. Furthermore, to investigate the relationship between Ne and solar activity, we also calculated the cross-correlation between Ne and F10.7. The correlation coefficients for each altitude are shown in Figure 5c for both the TIEGCM and TIEGCM-HME runs. The low correlation observed during this period was expected due to low solar activity. The correlation is positive, with a coefficient of less than approximately 0.5. However, the correlation decreases to about −0.3 above 250 km in the case of TIEGCM.

Compared to period 1, the variations in Ne simulated from the TIEGCM run, along with its difference from TIEGCM-HME, are shown in Figures 5d and 5e. During this period, the effect of solar activity on the electron density is clearly visible. In comparison to TIEGCM, the difference plot shows the influence of tidal forcing. Ne decreases by approximately 5%–15% between 230 and 330 km and increases by about 5%–10% above 350 km. In period 2, there appears to be a more pronounced correlation between solar activity and Ne in comparison to period 1. A maximum correlation coefficient of approximately 0.8 is evident below 200 km and above 300 km, with a slight decrease in correlation within the 200–300 km range. It is worth mentioning that the overall correlation ranges from 0.5 to 0.8 in period 2 (Figure 5f), representing an increase compared to the lower correlation observed during period 1.

In our effort to comprehend the significance of the O/N_2 ratio, we conducted a thorough examination of its variations throughout the study period and its correlation with the F10.7 index. Figures 6a and 6d illustrate the O/N_2 ratio simulated using the TIEGCM, while Figures 6b and 6e depict the percentage difference plot between the TIEGCM and TIEGCM-HME runs simulated O/N_2 ratio for both the periods at 0° longitude. To calculate the

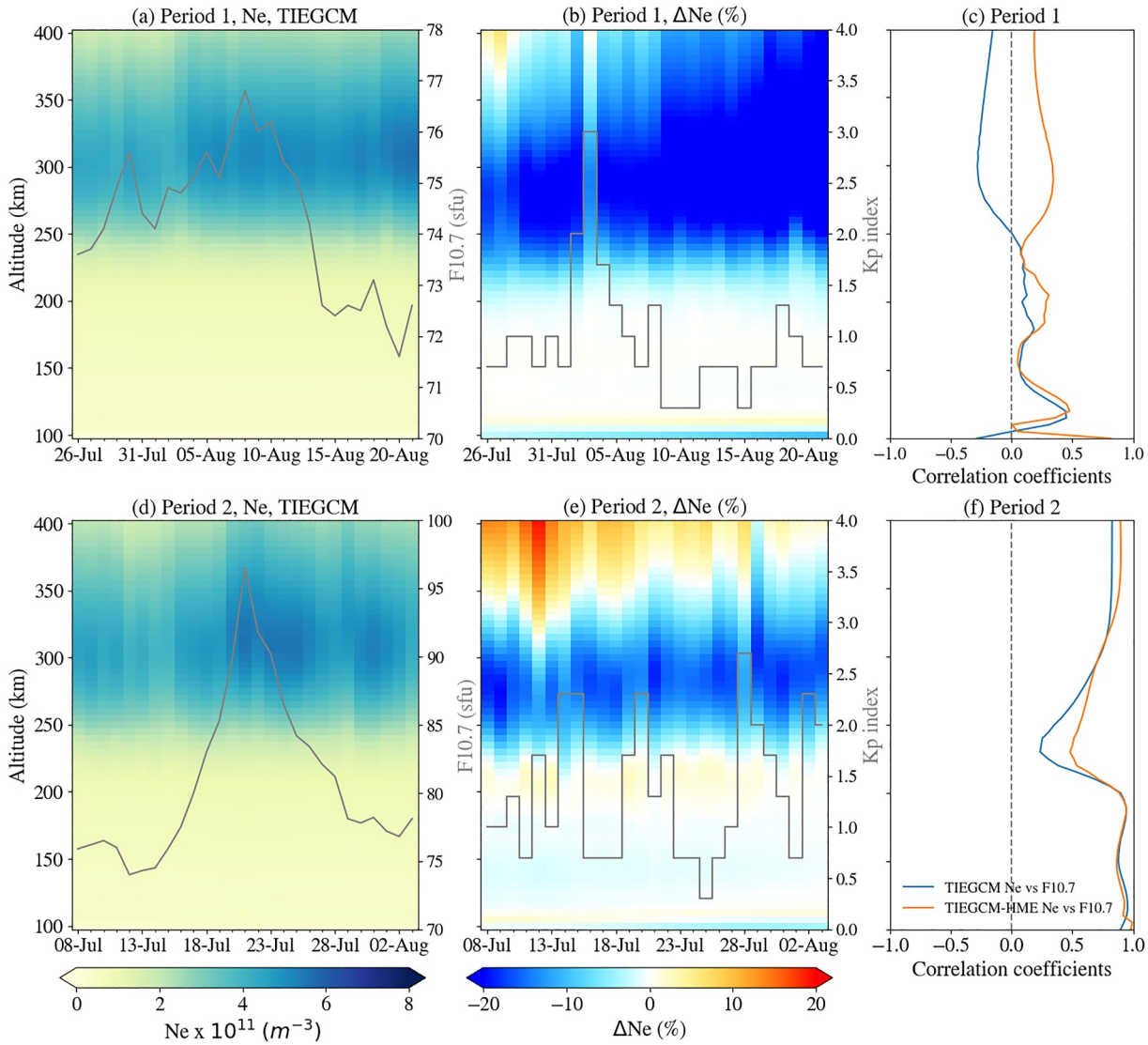

Figure 5. At 0°N, 0°E, the diurnal mean of Ne simulated by TIEGCM and its percentage difference ((TIEGCM-HME—TIEGCM)/TIEGCM) with Ne simulated by TIEGCM-HME are represented in (a, d) and (b, e) respectively. The gray curves in (a, d) represent the F10.7 index, while in (b, e) they represent the Kp index. The correlation coefficients of Ne with the F10.7 index are shown as altitude profiles in (c, f), where the blue (red) curves represent the correlation between TIEGCM Ne (TIEGCM-HME Ne) and the F10.7 index. The upper row (a–c) illustrates period 1, while the lower row (d–f) depicts period 2.

model O/N_2 ratio, we utilized the mmr of O and N_2. Here, mmr(N_2) is calculated by 1—mmr(O)—mmr(O_2). This suggests that N_2 is driven by the photodissociation of O_2, ionization of O/O_2, as well as their recombination, rather than by any actual interactions of O and N_2. During period 1, it is noted that the O/N_2 ratio shows an increase with altitude, reaching its peak above 350 km (Figure 6a). As compared to TIEGCM, in the case of TIEGCM-HME, the O/N_2 ratio experiences a decrease of approximately 1%–5% above 110 km (Figure 6b). An observed reduction in the O/N_2 ratio is attributed to tidal forcing (Forbes et al., 2024). In period 2, the O/N_2 ratio demonstrates an increase of approximately 3%–5% in the TIEGCM-HME model (see Figure 6e). This trend contrasts with period 1, where the O/N_2 ratio decreases due to tidal forcing. Period 1 experiences low solar activity, leading to dominance of tidal forcing, while period 2 is characterized by higher solar and geomagnetic activity, causing solar forcing to dominate. The combined impact of solar and tidal forcing results in an overall increase in the O/N_2 ratio during period 2. We have also calculated the cross-correlation of the O/N_2 ratio with the solar F10.7 index.

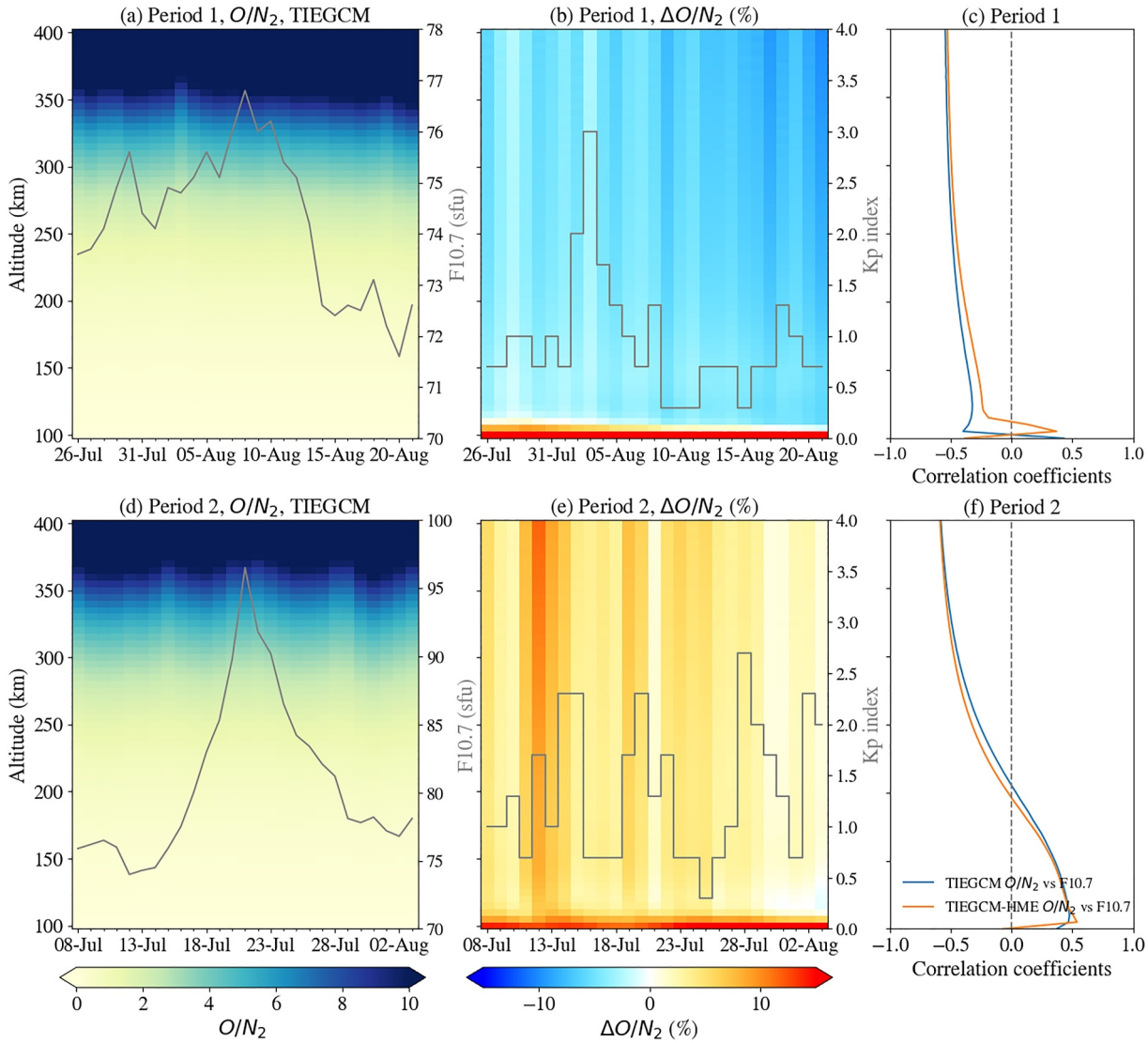

Figure 6. Same as shown in Figure 5, but for the O/N_2 ratio.

It was observed that a negative correlation exists for both the TIEGCM and TIEGCM-HME runs during period 1 (Figure 6c). Furthermore, during period 2, a positive correlation was noted below 200 km, with correlation coefficients in the range of approximately 0.1–0.5, decreasing with altitude. Above 200 km, the correlation coefficient is negative (Figure 6f).

To further explore the relationship between the daily mean O/N_2 ratio and Ne at varying altitudes, we conducted an analysis of cross-correlation coefficients at 0°E. The aim of calculating the correlation is to observe the relationship between changes in O/N_2 and Ne due to tidal forcing. Here, the substantial positive correlation between O/N_2 and Ne attributed to tidal forcing suggests that atmospheric tides significantly influence O/N_2 and the Ne in the ionosphere. Changes in the lower thermosphere due to tidal-induced modifications of the MLT circulation can also impact the electron density. The decrease in O and increase in N_2 in the lower thermosphere lead to higher altitudes through molecular diffusion, causing a reduction in (O/N_2) throughout the thermosphere (Jones et al., 2014). This reduced O/N_2 ratio influences the production and loss of O^+, which is the dominant ion in the F region, resulting in a decrease in electron density (Yamazaki & Richmond, 2013).

Figure 7 presents the correlation coefficients for period 1 and period 2 as a function of latitude and altitude. In Figure 7a, a correlation coefficient ranging from 0.5 to 0.9 is observed between 200 and 250 km, while below

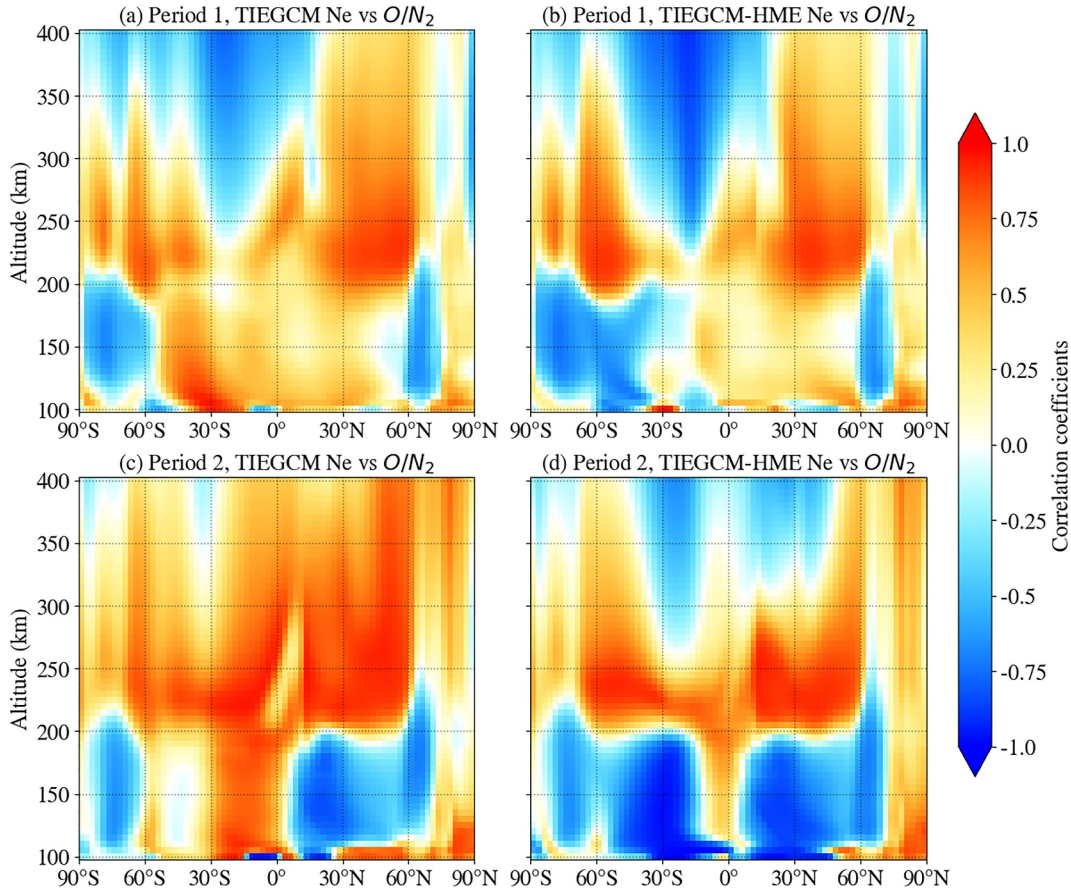

Figure 7. The correlation coefficients between the diurnal mean Ne and the O/N_2 ratio simulated by the TIEGCM (a, c) and TIEGCM-HME (b, d) at the 0°E geographic longitude are presented as a function of latitude and altitude. The upper (lower) row depicts period 1 (period 2).

200 km, a positive correlation ranging from 0.4 to 0.6 is evident between 60°S to 60°N. Furthermore, when comparing the TIEGCM run to the TIEGCM-HME run, a slight decrease in correlation is noted below 200 km. In the Northern Hemisphere (NH), the correlation remains consistent across all altitudes, whereas variations are noticeable in the SH, as depicted in Figure 7b. Figures 7c and 7d display the correlation coefficients between O/N_2 and Ne for period 2 for both TIEGCM and TIEGCM-HME runs. During period 2, the correlation coefficients above 200 km generally exceed 0.7, with a maximum of approximately 0.9. However, below 200 km, positive correlation is observed in the SH between 0° to 30°S, while negative correlation is observed in the NH and above 60° in the SH. When comparing TIEGCM to TIEGCM-HME, the overall correlation decreases above 250 km as well as below 200 km (Figure 7d). This decrease in correlation in both cases suggests a clear influence of the tidal forcing at both low and high altitudes.

Furthermore, to investigate the causality between O/N_2 and Ne, we aim to further explore the Granger causality method (Granger, 1969; Shojaie & Fox, 2022), a statistical hypothesis test used to establish whether one time series can be predictive of another. Our specific focus is on the potential of the O/N_2 ratio to forecast Ne. While cross correlation analysis indicates a relationship between the two, it does not provide insight into whether changes in O/N_2 precede or cause Ne changes, or if this relationship varies with time delays. Granger causality will enable us to ascertain whether past values of O/N_2 can predict Ne, particularly valuable if O/N_2 dynamics drive Ne changes with some delay. The result of a Granger causality test is a p-value. If the p-value is below 0.05, past O/N_2 values significantly improve TEC prediction. This will help us investigate the relationship between O/N_2 and Ne for both the model runs with and without HME tides. Figure 8a shows the TIEGCM O/N_2 Granger-cause Ne during period 1. P-values are generally below 0.05 above 250 km in the low-latitude region. Similar results are observed in the TIEGCM-HME run (Figure 8b), and values are statistically significant in low-latitude

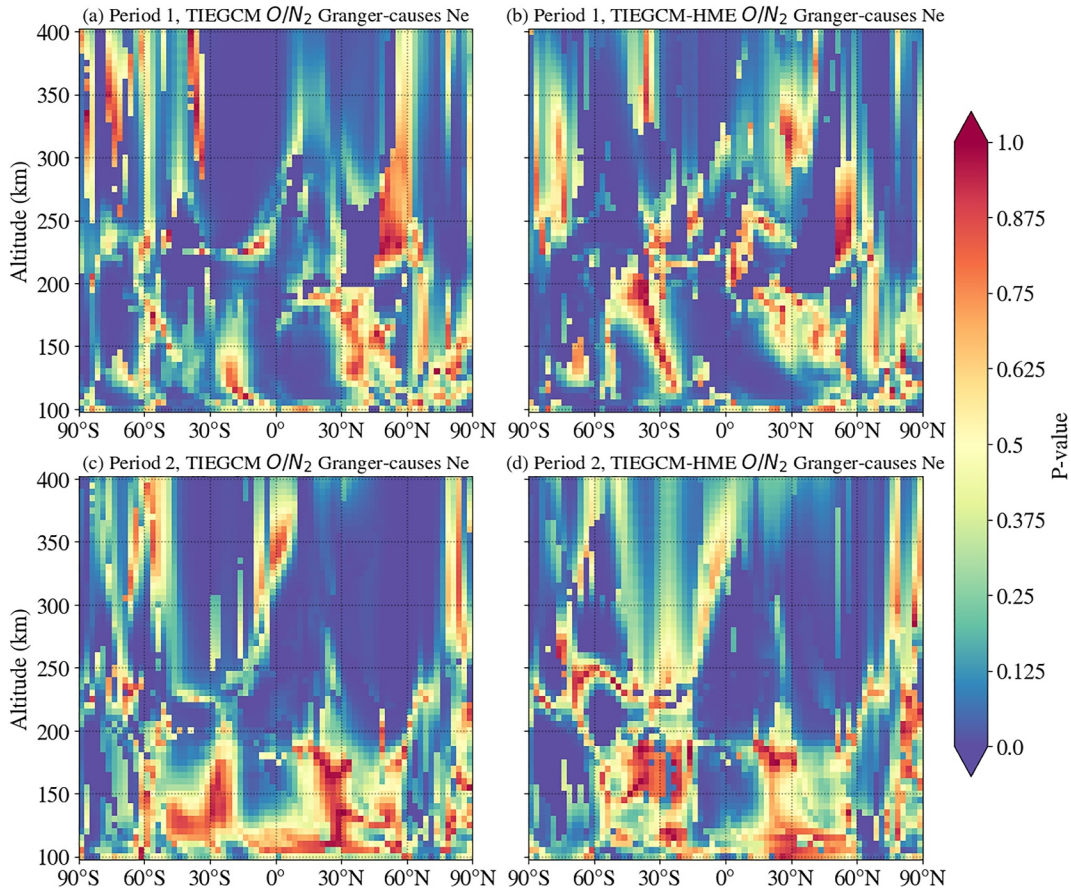

Figure 8. The Granger causality test between the diurnal mean Ne and the O/N_2 ratio simulated by the TIEGCM (a, c) and TIEGCM-HME (b, d) at the 0°E geographic longitude is presented as a function of latitude and altitude. The upper (lower) row depicts period 1 (period 2).

regions. *P*-values are not statistically significant below 200 km. The causality between TIEGCM O/N_2 and Ne during period 1 shows that the O/N_2 ratio controls the Ne variability. However, including tidal forcing leads to a reduction in causality in the mid-latitudes. During period 2, the test is still statistically significant in the low latitude region above 300 km in the NH (Figures 8c and 8d), indicating that O/N_2 drives changes in Ne.

Based on the altitude-based correlation analysis, we observe that tidal forcing clearly contributes to the correlation between O/N_2 and Ne. To gain a better understanding of the global impact of tidal forcing, we will further investigate the global distribution of correlation coefficients between NmF2 and the corresponding O/N_2 ratio for both the TIEGCM and TIEGCM-HME runs as depicted in Figure 9 for both periods 1 and 2. We have calculated the NmF2, and the O/N_2 ratio at the height of the peak electron density. This analysis enables us to compare the relationship between NmF2 and the O/N_2 ratio, which is an indicator of composition changes in the TI region. The correlation map shown in Figure 9a demonstrates a complex relationship between TIEGCM NmF2 and O/N_2 during period 1. In the low-latitude region, the correlation is generally positive, ranging from 0.6 to 0.9. However, in the mid-latitude region, the correlation is mostly positive in the NH with correlation coefficients of 0.3–0.7 except for the western American and the Mediterranean region. Conversely, more regions of negative correlation are observed in the mid- and high-latitudes in the SH, with correlation coefficients ranging from −0.3 to −0.7. Comparatively, for TIEGCM-HME, the correlation undergoes significant changes due to tidal forcing, specifically in the SH, where the correlation decreases to about −0.5 to −0.9. As solar activity is very low during period 1, the impact of tidal forcing becomes evident in the correlation (Figure 9b). Figure 9c shows the correlation coefficient between TIEGCM NmF2 and O/N_2 during period 2. In comparison to period 1, the correlation is lower during period 2, ranging from maxima of 0.2 to 0.6 in the low- and mid-latitudes. Negative correlation is observed in the auroral region, as well as in the region between 70°W and 180° in the low- and mid-latitudes. In

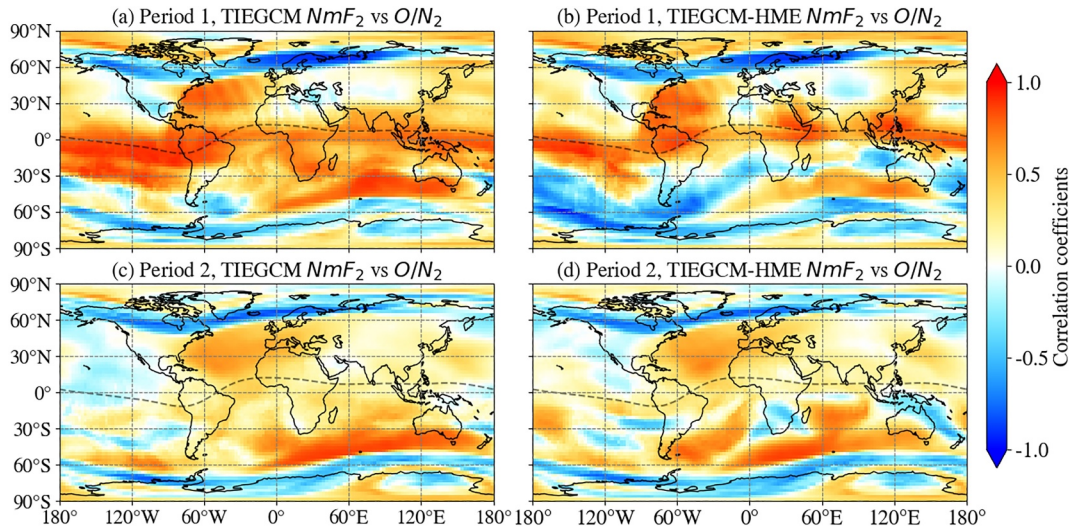

Figure 9. Global distribution of correlation coefficients between diurnal mean NmF2 and corresponding O/N_2 simulated by TIEGCM (a, c) and TIEGCM-HME (b, d). The upper panels represent period 1, and the lower panels show period 2.

contrast to TIEGCM, the correlation for TIEGCM-HME run demonstrates complex behavior. During the tidal forcing run, the correlation changes in the low- and mid-latitudes, and a negative correlation is observed in some patches in the SH (Figure 9d). This suggests complex influence of tidal forcing.

In the present study, we investigate the influence of tidal forcing on both the NmF2 and O/N_2. Figure 9 shows that the impact of tidal forcing is primarily observed in the low- and mid-latitude regions, which changes the correlation between O/N_2 and NmF2. Previously, Jones et al. (2014) and Maute et al. (2023) investigated the influence of tidal forcing using TIEGCM simulations. Maute et al. (2023) reported a 15%–20% change in the zonal and diurnal mean NmF2 with a roughly 10% modification in the O/N_2 ratio from 7 August to 26 September 2020, associated with strong tidal and background variations. Jones et al. (2014) also reported the changes in composition using the TIEGCM forced with and without the tidal forcing, finding a 20% decrease in NmF2 and a 4% decrease in O/N_2 due to the inclusion of tides in August–September. Vaishnav, Jacobi, et al. (2021) showed that the changes in the TEC are associated with variations in the simulated O/N_2 ratio using CTIPe model simulations.

3.3. Delayed Ionospheric Response

It is widely known that the TI system reacts to solar activity with a delay ranging from a few hours to a few days, depending on the analysis method and data set resolution. Various authors have reported that different delays are observed for several TI parameters, including Ne, O/N_2 ratio, neutrals, and TEC. This delay is typically caused by an imbalance between production and loss processes, as discussed by Ren et al. (2019, 2020). Recently, Schmölter et al. (2020) focused on observations from solar cycles 24 and 25 to investigate the ionospheric delay, providing a temporal and spatial evolution of the delay and its connection to geomagnetic activity. Vaishnav et al. (2019) provided an overview on the relationship between TI and solar activity using several solar proxies and showed that the ionospheric delay response is verifiable using any of the available solar proxies. However, calculating precise delays can be challenging due to the unavailability of high-resolution data sets. Therefore, TI models are used to understand the physics behind the ionospheric delay and explore internal mechanisms. Ren et al. (2019, 2020) and Vaishnav, Jacobi, et al. (2021) used global 3-D models to provide comprehensive information on delayed responses to solar variability. Their modeling results highlight the role of loss and production mechanisms, as well as transport processes, along with various factors that can affect the TI system, such as geomagnetic and lower atmospheric forcing.

We are embarking on a new investigation into the ionospheric delay. Our analysis incorporates observations and TIEGCM simulations with and without tidal forcing. To calculate the ionospheric delay, we use cross-correlation analysis (Vaishnav, Jacobi, et al., 2021). We utilize SOHO/SEM EUV flux and F10.7 to calculate the ionospheric

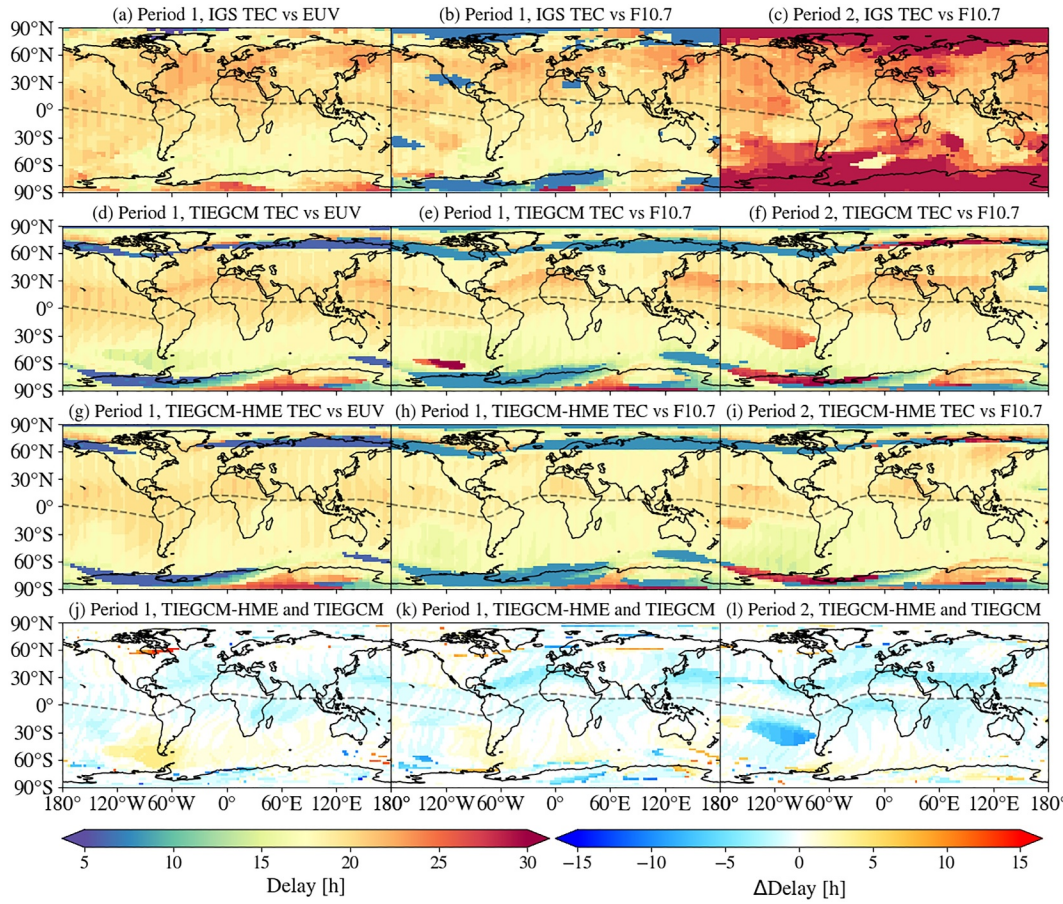

Figure 10. The ionospheric delay global maps are organized as follows: The upper panels display IGS TEC versus EUV (a) and F10.7 (b, c). The second row shows TIEGCM TEC versus EUV (d) and F10.7 (e, f), while the third row presents TIEGCM-HME versus EUV (g) and F10.7 (h, i). In the lower panels (j–l), the difference between the delay calculated for TIEGCM-HME and TIEGCM simulated TEC versus EUV/F10.7 is shown. The left and central panels display ionospheric delay maps for period 1, while the right panels display ionospheric delay maps for period 2.

delay. The EUV observations are restricted to period 1 only, with some missing values. Unfortunately, EUV observations are not available for period 2. Due to solar EUV observational limitations, we utilized the F10.7 index for delay calculation, which is also used as a solar activity proxy in model simulations. Another advantage of using the F10.7 index is that the delay calculated using the F10.7 index aligns with the delay reported in the majority of preceding studies (Ren et al., 2018; Schmölter et al., 2020; Vaishnav, Jacobi, et al., 2021). For the delay calculation, the F10.7 index was linearly interpolated to a time interval of 1 hr to obtain the hourly time series. Furthermore, any missing values in the EUV timeseries for period 1 were interpolated using linear interpolation.

Figure 10 depicts the ionospheric delay between EUV/F10.7 and observational, TIEGCM, and TIEGCM-HME TEC. Figure 10a illustrates the ionospheric delay maps calculated between observed TEC and EUV during period 1. The mean ionospheric delay is approximately 19 hr, with a delay of about 17–22 hr in the low- and mid-latitude region. The delay decreases in the high-latitude region to less than 12 hr. A longer delay is observed in the NH than in the SH. The TIEGCM simulated TEC shows similar delay with a mean delay of about 18 hr but with strong differences at auroral latitudes characteristics (Figure 10d). However, hemispheric differences are observed in both the observed and modeled delay. The overall delay calculated using TIEGCM modeled TEC shows similar latitudinal behavior as seen in the observed TEC.

Additionally, we computed the delay for the TIEGCM-HME run, as shown in Figure 10g. We observed differences in magnitude compared to the observed delay and TIEGCM. The mean ionospheric delay is approximately 17 hr, with a delay of about 17–20 hr in the low- and mid-latitude region. To further examine the influence

of tidal forcing on ionospheric delay, we calculated the delay difference between the TIEGCM-HME and TIEGCM runs, as depicted in Figure 10j The difference plot shows that the ionospheric delay decreases by 1–4 hr using tidal forcing in low-latitude regions during period 1 and increases by 1–5 hr in the SH mid-latitude. This difference in modeled delay demonstrates the impact of tidal forcing on delay estimation.

Similar to the left panels, the middle panels of Figure 10 depict the delay maps calculated using the F10.7 index instead of EUV. This is aimed at investigating the differences and the validity of utilizing the F10.7 index when EUV data is unavailable. In Figure 10b, the ionospheric delay maps between observed TEC and F10.7 during period 1 are illustrated. The average ionospheric delay is around 18 hr, with the maximum delay in the low- and mid-latitudes region. The delay decreases to less than 10 hr in the high-latitude region. When compared to EUV, the delay calculated with F10.7 exhibits similar variations except for high latitudes and can partly reproduce a similar delay as observed with the EUV (Figure 10a). This allows us to use the F10.7 index for calculating ionospheric delay when solar EUV flux observations are unavailable. While there are some differences in magnitude, the overall global distribution pattern remains similar. There are some patches with lower delays of about 5–7 hr that can be seen in mid- and high-latitude regions.

The TIEGCM simulated TEC shows similar delay characteristics, with a mean delay of about 17 hr (Figure 10e), with a delay of about 16–22 hr in the low- and mid-latitudes region. The delay decreases in the high-latitude region to less than 15 hr. Furthermore, we calculated the delay for the TIEGCM-HME run, as shown in Figure 10h. The average ionospheric delay is around 16 hr. The differences between the observed and TIEGCM-HME modeled delays are reduced compared to the TIEGCM run. Similar to Figure 10j, the difference plot (Figure 10k) indicates that the ionospheric delay decreases by 1–5 hr in low-latitude region during period 1 when tidal forcing is used, and increases by 1–5 hr in the SH mid-latitudes.

In the right column, similar delay maps have been shown for period 2. Figure 10c displays the ionospheric delay between observed TEC and F10.7. The mean delay during period 2 is longer compared to period 1 due to slightly higher solar activity and it varies from 12 to 30 hr. Longer delay is observed in the high-latitude region, with a maximum of about 25–30 hr. Comparing the observed delay with the TIEGCM modeled delay, we note that the modeled delay is longer in the low-latitude region, with a mean delay of about 18 hr (Figure 10f). For the TIEGCM run, the ionospheric delay varies from 7 to 25 hr. The bias in the low-latitude between observed and TIEGCM modeled delay is about 1–6 hr. However, this bias increases in the case of the TIGECM-HME run (Figure 10i). The mean ionospheric delay for the TIGECM-HME run is approximately 17 hr, with a delay of about 16–20 hr in the low- and mid-latitude region. In the region spanning from 70°W to 140°W in the low- to mid-latitudes, the delay decreases to ≈4–7 hr in the case of TIEGCM-HME in comparison to TIEGCM. During period 2, the ionospheric delay is successfully reproduced in the low- and mid-latitudes. However, in the high-latitude region, the estimated delay is lower compared to the one based on observed TEC. The differences between the TIEGCM and TIEGCM-HME estimated delay period 2 are shown in Figure 10l. The difference map shows that the delay decreases in the low- and mid-latitude regions by about 1–8 hr and slightly increases in the high-latitude region.

To quantitatively assess the performance of TIEGCM and TIEGCM-HME, we used the root mean square error $\left(RMSE = \sqrt{\frac{1}{n}\sum_{i=1}^{n}\left(y_{obs} - y_{mod}\right)^2}\right)$ calculation, where, y_{obs} and y_{mod} represent observed and modeled estimated delay, respectively. Based on the observed and modeled delay (illustrated in Figure 10), we calculate the RMSE for both study periods. During period 1, the RMSE between IGS and TIEGCM estimated delays using EUV is about 4.5 hr, and it slightly decreases to about 4.3 hr with TIEGCM-HME. The RMSE between IGS and TIEGCM estimated delays using F10.7 is about 5 hr, and it decreases to about 4.6 hr with TIEGCM-HME. For low- and mid-latitudes, the RMSE values are about 3.3 hr and about 3.1 hr in the case of TIEGCM and TIEGCM-HME delays using F10.7, while for EUV it was 3.07 hr for TIEGCM and reduced to 2.70 hr for TIEGCM-HME, respectively. During period 2, the RMSE for both runs is approximately 8 hr, while for low- and mid-latitudes, the RMSE is approximately 4.6 hr.

The ionospheric delay exhibit variability across different regions. As a result, the RMSE values have been computed for a grid resolution of 10°/20° in latitude and longitude. Figure 11 illustrates the RMSE values comparing the observed delay with the modeled delay shown in Figure 10. The upper panels of Figure 11 depict the RMSE in the case of observed and modeled delay calculated using EUV during period 1 (Figures 10a, 10d,

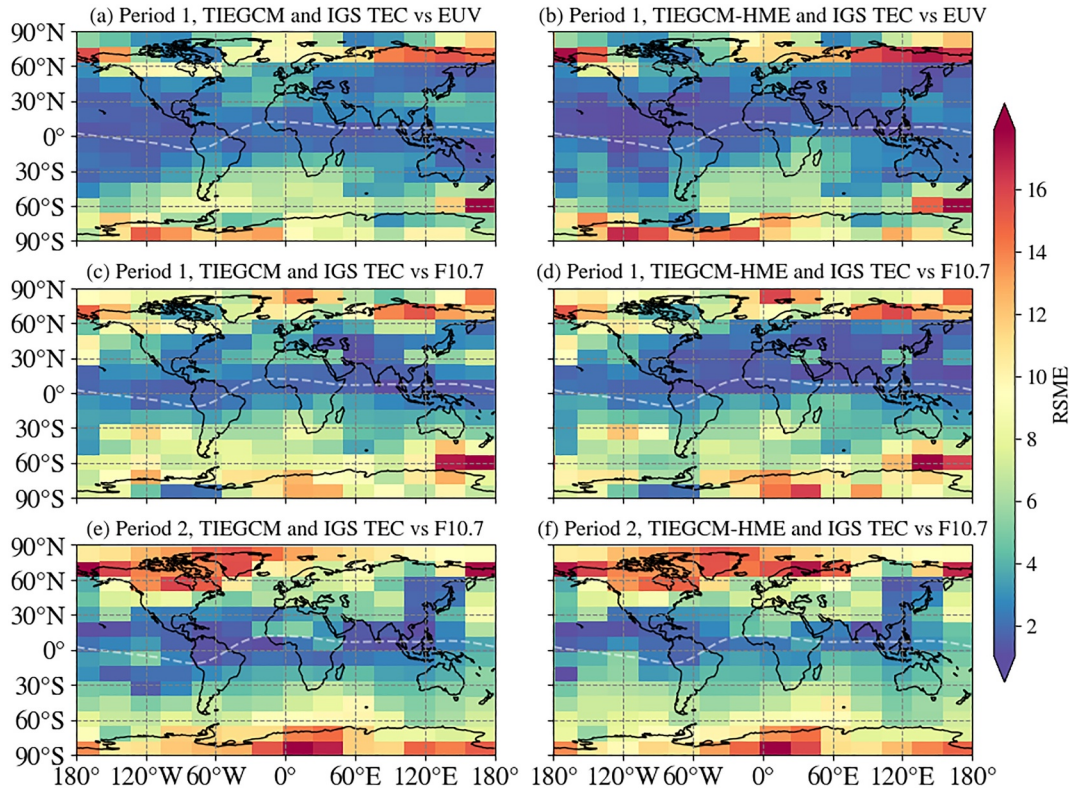

Figure 11. The RMSE maps are as follows: (a, c, e): IGS versus TIEGCM delay using EUV (period 1), F10.7 (period 1), and F10.7 (period 2), respectively. (b, d, f): IGS versus TIEGCM-HME delay using EUV (period 1), F10.7 (period 1), and F10.7 (period 2), respectively. The upper and middle panels display RMSE maps for period 1, while the lower panels display maps for period 2. The RMSE values are calculated at a grid resolution of 10° in latitude and 20° in longitude.

and 10g). The RMSE values are notably small in the low- and mid-latitude region, and it increases in the high-latitude region. In Figure 11a, the RMSE values range from 0.5 to about 2 hr in the low- and mid-latitude region, and 2–8 hr in the high-latitude region. Similar variations can be observed in Figure 11b, where the RMSE values are slightly lower, ranging from about 0.5 to 2 hr. In the region spanning from 70°W to 120°W in the low- to mid-latitudes, the RMSE decreases to ≈1 hr in the case of TIEGCM-HME in comparison to TIEGCM. In general, the lower RMSE values are observed in the NH in both the TIEGCM and TIEGCM-HME runs. In the middle panels of Figure 11, the RMSE for the observed and modeled delay calculated using F10.7 during period 1 is shown (Figures 11c and 11d). When comparing to EUV, the RMSE values for F10.7 are slightly comparable in the low-latitude and mid-latitude NH region, but they increase in the SH by about 2–4 hr. Compared to TIEGCM (Figure 11c), the RMSE reduced slightly, ranging from about 0.5 to 3 hr in the low latitude and mid-latitude in the case of TIEGCM-HME (Figure 11d). In the lower panels of Figure 11, the RMSE in the case of observed and modeled delay calculated using F10.7 during period 2 is shown (see Figures 10c, 10f, and 10i). Period 2 demonstrates more complex behavior compared to period 1. During period 2, the RMSE values range from 1 to 6 hr in low- and mid-latitude regions and show stronger variations in the high-latitude region, with a maximum of about 15 hr. In Figure 11e, in the case of TIEGCM, the RMSE values are comparable to period 1 in the low- and mid-latitude region. However, the values increase to about 2–4 hr in the high-latitude region. Comparing TIEGCM (Figure 11e) to TIEGCM-HME (Figure 11f), the RMSE values are comparable and increase slightly by about 0.5–2 hr in the low- and mid-latitudes, while they decrease by about 1 hr in the high-latitude region.

During period 1, it appears that the RMSE is generally reduced in the case of TIEGCM-HME compared to TIEGCM, indicating a slight improvement in the ionospheric delay estimation. However, during period 2, the RMSE values slightly increased in the low- and mid-latitude regions for the TIEGCM-HME run. Based on the findings, tidal forcing leads to a slight decrease in ionospheric delay compared to the TIEGCM run, but it also increases the bias with the observed delay.

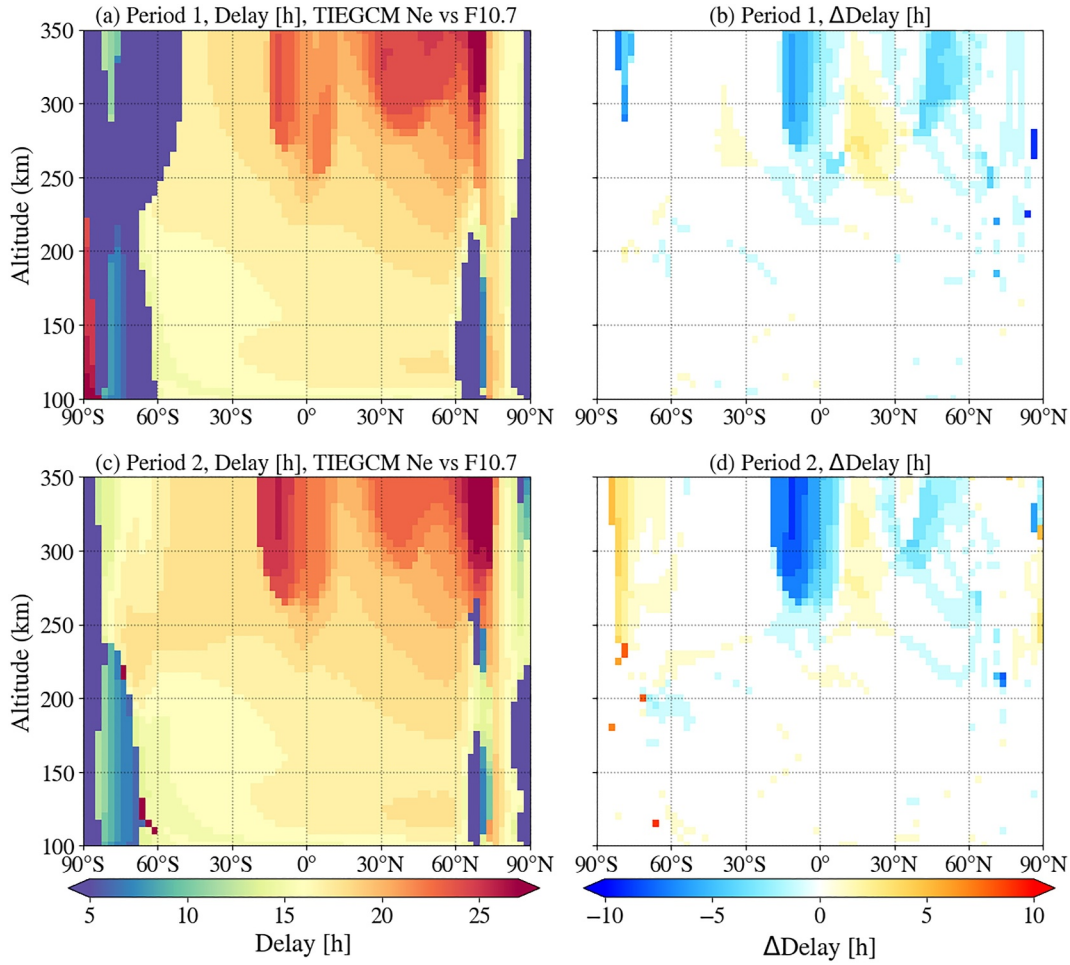

Figure 12. The latitude and altitude distribution of the ionospheric delay at 0°E between TIEGCM Ne with F10.7 (a, c) and its difference with delay estimated between TIEGCM-HME Ne with F10.7 (b, d). The upper panels show delay distribution for period 1, while the lower panels show delay distribution for period 2.

It has been observed that including tidal forcing can affect the ionospheric delay differently depending on the latitude. At low-latitudes, the delay tends to decrease by as much as 1–6 hr, while at mid- and high-latitudes it tends to increase by up to 1–5 hr mainly in SH. This suggests that tidal forcing has non-negligible impact on the ionospheric delay and should be taken into account when analyzing such phenomena, specifically during low solar activity.

We have also calculated the ionospheric delay between F10.7 and NmF2 for both periods and both the TIEGCM and TIEGCM-HME runs. We found similar characteristics to TEC and a slightly longer delay in the low-latitude region (Figure not shown).

The distribution of the ionospheric delay between TIEGCM Ne and F10.7 at 0°E is shown in Figure 12 as a function of latitude and altitude for period 1 and period 2. The maximum delay is about 23 hr at an altitude of 300 km (Figure 12a). Below 250 km, the delay is around 19 hr. The delay increases with altitude and is longer in the NH. The findings are consistent with previous research, much of which has been based on artificially simulated experiments (e.g., Schmölter et al., 2022; Vaishnav, Jacobi, et al., 2021). In the high-latitude region, there is an observed lower ionospheric delay of approximately 5–10 hr. In Figure 12b, the comparison between the ionospheric delay calculated between Ne and F10.7 in TIEGCM and TIEGCM-HME is presented. Below 250 km, the ionospheric delay generally remains relatively stable, but exhibits slight reductions at specific locations by approximately 1 hr when using TIEGCM-HME. However, in the F-region above 250 km, the delay experiences an increase of about 1–3 hr in the low-latitude region of the NH. Furthermore, in the SH at low-latitudes and in the

NH at mid-latitudes, the delay shows a decrease of approximately 3–5 hr. The lower row displays the ionospheric delay during period 2. In Figure 12c, the delay for the TIEGCM run shows a maximum delay of about 27 hr in the low- and mid-latitude region of the NH. The delay in the high-latitudes, specifically in the SH, is about 5–10 hr below 250 km. In comparison to the TIEGCM run, during the TIEGCM-HME run, the ionospheric delay decreases to 10 hr in the low-latitude region above 260 km, while the delay increases to 3–5 hr in the SH high-latitude (Figure 12d). The observed pattern is similar in both the study periods; however, the difference observed in the decrease in delay during period 2 is higher, about 5 hr as compared to period 1.

At the electron density peak, photoionization dominates due to strong EUV absorption, while photodissociation dominates in the lower ionosphere. This leads to the production of additional oxygen in the lower ionosphere, which through transport contributes to an increase of O and O^+ at the F-region peak, resulting in a delay of the electron density response to changes in solar EUV flux (Schmölter et al., 2022; Schmölter & von Savigny, 2022). It is worth noting that current investigations have shed light on the significant role that lower atmospheric forcing play in contributing to changes in ionospheric delay using more realistic model simulations. Additionally, a previous study by Vaishnav, Jacobi, et al. (2021) suggested the impact of transport processes on ionospheric delay.

Upon thorough analysis of Figure 7b, it is apparent that there exists a noteworthy negative correlation between changes in NmF2 and O/N_2 in the low-latitude region of the SH above 300 km during period 1 for the TIEGCM-HME as compared to TIEGCM run. In the same region, the ionospheric delay diminishes by approximately 1–5 hr (Figure 12b). Subsequently, during the period 2 (Figure 7d), characterized by slightly higher solar activity compared to period 1, the correlation coefficient experiences a marginal reduction to approximately −0.5, resulting in a substantial decrease in the ionospheric delay by about 2–8 hr in the low-latitude region of the SH (Figure 12d). Furthermore, according to the Gragner causality test, the low latitude region is statistically significant above 300 km (Figure 8b). This demonstrates the impact of tidal forcing on the composition of the thermosphere, resulting in changes in ionospheric delay.

3.4. Relationship Between TI and Solar/Geomagnetic Activity

Through the current investigation, it has been noticed that lower atmospheric forcing play a crucial role in the ionospheric delay. The analysis revealed that there is a strong correlation between NmF2 and O/N_2 at low-latitudes. This suggests that delay observed in the NmF2 could also be related to a delay in the O/N_2 ratio. Vaishnav et al. (2024) investigated the ionospheric delay using CTIPe model simulations and GOLD observations. Their findings revealed that the positive correlation between the O/N_2 ratio and solar flux is only present in the NH which explains the delay in TEC. They also suggested that the negative correlation at other latitudes may be caused by lower atmospheric forcing and geomagnetic activity. Therefore, to investigate the relationship between these parameters, we calculate the cross correlation of IGS TEC and GOLD O/N_2 ratio with F10.7 and Kp index during the study period.

Figure 13 displays the correlation maps calculated using IGS TEC, O/N_2, and F10.7 during period 1 and period 2. Figure 13a illustrates the correlation between IGS TEC and F10.7. The correlation is positive in the low- and mid-latitude regions, with correlation coefficients ranging from about 0.4 to 0.6. In the high latitude region of the SH, a negative correlation of about 0.4 is observed. The overall correlation is low due to lower solar activity. Other dominant forcing, such as lower atmospheric forcing, could be the reason for the lower correlation. In addition, Figure 13b shows the correlation map during period 2. In comparison to period 1, the overall correlation is positive, ranging from about 0.3 to 0.8, with the maximum correlation in the low-latitude region. Due to slightly higher solar activity than in period 1, a strong correlation is observed during period 2. The second row of Figure 13 displays the correlation between O/N_2 and F10.7. The correlation map during period 1 shows a negative correlation in the NH, whereas a positive correlation of about 0.3–0.7 is observed in the SH. In contrast to period 1, the overall correlation during period 2 between O/N_2 and F10.7 is negative, ranging from −0.2 to −0.6 (Figure 13d). Furthermore, we calculated correlation coefficients between IGS TEC, O/N_2, and Kp index. Figure 13e shows the correlation map between IGS TEC and Kp index during period 1. Since solar activity is very low during the selected period, the role of other forcing becomes dominant, such as geomagnetic and lower atmospheric forcing. Here, the role of geomagnetic activity becomes evident. The correlation is generally positive in the low- and mid-latitude regions, while negative correlation is observed in the high latitude region in the SH. Compared to period 1, during period 2, the correlation between IGS TEC and Kp slightly decreases. During this period, there is a slight increase in solar

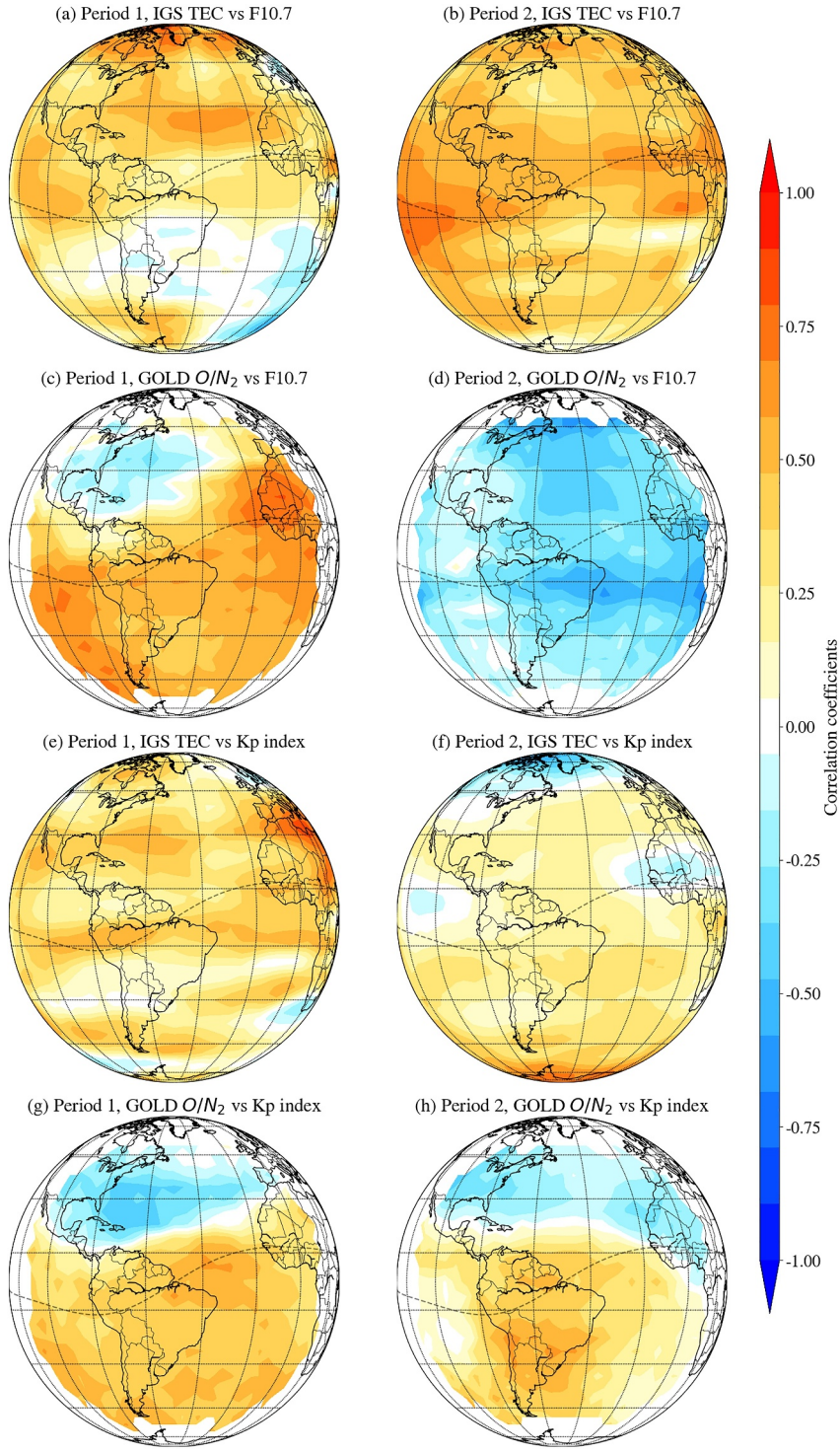

Figure 13. The correlation coefficient maps are as follows: (a, b) IGS TEC versus F10.7, (c, d) GOLD O/N_2 versus F10.7, (e, f) IGS TEC versus Kp, and (g, h) GOLD O/N_2 versus Kp. The left panels display correlation maps for period 1, while the right panels display correlation maps for period 2.

activity, but it is still dominated by geomagnetic activity, so a correlation coefficient with the Kp index is expected (Figure 13f). The lower panels show correlation maps of O/N_2 and Kp index. The correlation maps show negative correlation in the NH in low- and mid-latitude regions. However, in other regions, the overall trend is positive, with

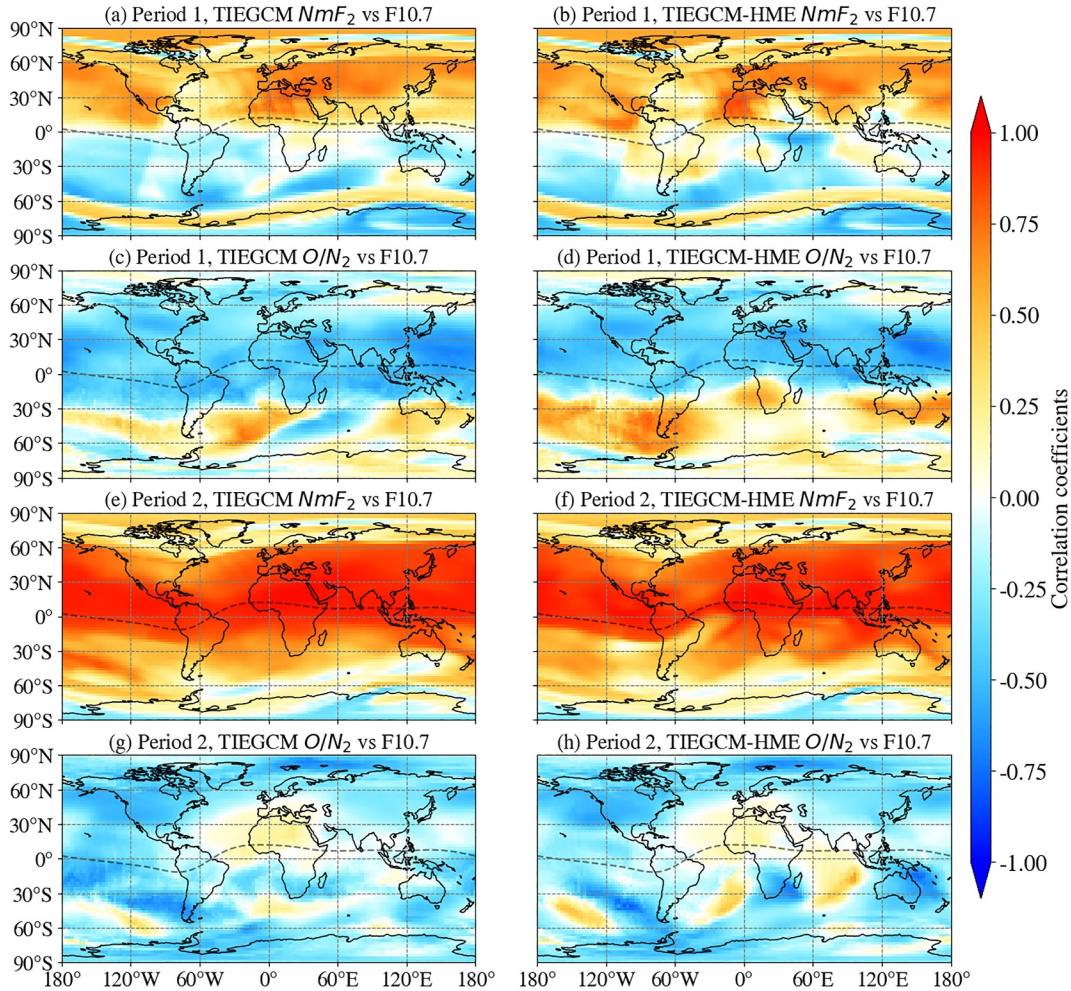

Figure 14. The correlation coefficient maps are as follows: (a, b) NmF2 versus F10.7 for period 1, (c, d) O/N_2 versus F10.7 for period 1, (e, f) NmF2 versus F10.7 for period 2, and (g, h) O/N_2 versus F10.7 for period 2. The left panels display correlation maps for the TIEGCM, while the right panels display correlation maps for the TIEGCM-HME.

a maximum correlation of approximately 0.5 in the low-latitudes and the SH as shown in Figure 13g, suggesting a O/N_2 dependence on solar activity (e.g., Schmölter et al., 2021; Zhang & Paxton, 2011). Compared to period 1, during period 2, the spatial pattern in correlation is the same, however, with lower correlation coefficients (Figure 13h). However, in other regions, the overall trend is positive, with a maximum correlation of approximately 0.5 in the low-latitudes and the SH, suggesting a O/N_2 dependence on solar activity (e.g., Schmölter et al., 2021; Zhang & Paxton, 2011). Cai et al. (2021) found that even during quiet geomagnetic activity, the electron density could be enhanced. Figure 1 illustrates the levels of solar and geomagnetic activity and indicates that geomagnetic activity potentially has a greater influence on the TI; therefore, O/N_2 is positively correlated with geomagnetic activity.

Based on our results, it is evident that during low solar activity, other factors like geomagnetic activity and lower atmospheric forcing have a greater impact on the TI. To delve deeper into this, we utilized the TIEGCM and TIEGCM-HME model simulations to investigate the contribution of lower atmospheric forcing. In Figures 14a–14d, correlation maps of NmF2 with solar activity (Figures 14a and 14b) and geomagnetic activity (Figures 14c and 14d) for period 1 are displayed. The correlation map of NmF2 with F10.7 during period 1 indicates a positive correlation in the NH, with correlation varying from 0.3 to 0.7. Despite the very low solar activity, we calculated the cross-correlation using daily data sets, which slightly improved the correlation. In the SH, the correlation is negative, with correlation coefficients ranging from −0.2 to −0.5 (Figure 14a). When compared to the TIEGCM run, the spatial distribution during the TIEGCM-HME run is almost similar; however, the overall correlation is

slightly decreased in the low-latitude region (Figure 14b). There is a noticeable increase in correlation in the low-latitude region, particularly in the SH low-latitude region. Importantly, these maps are consistent with the correlation map of IGS TEC versus F10.7 as shown in Figure 13a. The second row of Figure 14 displays the correlation maps of O/N_2 ratio with F10.7 for both TIEGCM and TIEGCM-HME runs. A negative correlation is observed in the NH and low-latitude region. In comparison to TIEGCM, the correlation significantly improves in the SH mid-latitude region, and the correlation coefficients vary from about 0.2 to 0.6. However, when compared to the correlation calculated from the GOLD observed O/N_2 and F10.7 (Figure 13c), the correlation is negative in the low-latitude region. Except for this, the correlation pattern is reproduced in the TIEGCM-HME run in the mid- and high-latitudes. In the third row of Figure 14, the correlation maps for period 2 are displayed. During this period, the maximum correlation observed between TIEGCM NmF2 and F10.7 is about 0.9. The correlation is generally positive, with higher correlation observed in the NH and lower correlation observed in the high-latitude region. In comparison to the TIEGCM run, the correlation is slightly decreased in the SH for the TIEGCM-HME run. As the solar activity is slightly higher than in period 1, the correlation is expected to improve, and indeed, higher correlation is observed. Furthermore, compared to the correlation calculated with IGS TEC and F10.7, the model-simulated correlation is high, although it reproduces the spatial pattern. For both periods, the correlation maps generally reproduce, with differences in correlation coefficients. The lower row of Figure 14 displays the correlation maps between the O/N_2 ratio and F10.7 for period 2. A negative correlation is generally observed for the TIEGCM and TIEGCM-HME. However, a slight positive correlation is observed in the low- and mid-latitude regions with correlation coefficients about 0.1–0.3. The spatial distribution is generally consistent with the correlation calculated with the GOLD observed O/N_2 ratio.

Upon analyzing both the observed and modeled parameters of the TIEGCM and TIEGCM-HME, it is evident that correlation maps calculated from the model simulated parameters are consistent with the correlations calculated from the observed parameters. Although there are discrepancies in certain regions, but overall characteristics can be more closely reproduced with the TIEGCM-HME. It is also worth noting that model simulations capture patterns during both solar activity levels.

4. Discussion and Conclusions

We examined the impact of lower atmospheric forcing on upper atmospheric variability using the Thermosphere-Ionosphere-Electrodynamics General Circulation Model (TIEGCM). We utilized numerical experiments comparing induced variability due to HME tides using constrained middle atmospheric winds and temperatures from ICON-MIGHTI observations to investigate the impact of tidal forcing on composition (Ne, NmF2, TEC and O/N_2 ratio) and delayed ionospheric variability.

This study aims to shed light on the impact of tidal forces on Ne profiles. It is important to note that during low solar and geomagnetic activity, lower atmospheric forcing significantly influences the distribution of Ne. However, Ne is primarily influenced by solar activity during periods of high solar activity.

A recent study by Vaishnav et al. (2024) suggested that lower atmospheric forcing may affect the ionospheric delayed response during low solar activity. As a result, our investigation focuses on analyzing ionospheric behavior during these times using simulations with and without tidal forcing. In this study, we investigated the impact of upward-propagating tides on the ionospheric delay during two specific periods: from 26 July to 21 August 2020 (period 1) and from 8 July to 3 August 2021 (period 2). The analysis suggests that tidal forcing significantly influences the TI composition, resulting in an approximate 15%–20% change in Ne at altitudes above 250 km. This change is attributed to tidal forcing during period 1 (Figure 5). Additionally, compared to period 1, there was an increase in Ne at higher altitudes above 350 km during period 2 and decreases about 5%–15% between 230 and 330 km. In comparison to Ne, the O/N_2 ratio also decreases to about 1%–5% above 110 km during period 1. The increasing tidal activity affects the atmospheric composition by altering the loss of O_2 through photodissociation and the recombination of O, resulting in changes in molecular oxygen and molecular nitrogen. This causes a decrease in atomic oxygen at all altitudes above 100 km due to molecular diffusion. As a result, it impacts the overall O/O_2 and O/N_2 ratios (Qian et al., 2009; Rees & Fuller-Rowell, 1988; Vaishnav, Jacobi, et al., 2021).

The cross-correlation analysis revealed a significant correlation between the NmF2 and the O/N_2 ratio at peak electron density height, as simulated by TIEGCM and TIEGCM-HME. Furthermore, the results indicated that the influence of tidal forcing is predominantly observed in the low- and mid-latitude regions, contributing to the

correlation between O/N_2 and NmF2. Our results are consistent with previous studies (Jones et al., 2014; Maute et al., 2023). Maute et al. (2023) observed a 15%–20% change in the zonal and diurnal mean NmF2 with a roughly 10% modification in the O/N_2 ratio during 7 August to 26 September 2020, associated with strong tidal and background variations.

We undertook an analysis to examine the ionospheric delayed response between the EUV/F10.7 and observed TEC. This was then compared with the delay calculated from TEC simulated using the TIEGCM and TIEGCM-HME runs. Following a correlation analysis, we identified a mean ionospheric delay of approximately 19 hr between observed TEC and EUV. It was observed that this delay is longer in low- and mid-latitude regions and shorter in high-latitude regions during period 1. When comparing TIEGCM TEC with TIEGCM-HME TEC, we noted that the ionospheric delay between TIEGCM-HME TEC and EUV shows a similar distribution, albeit with a slightly increased magnitude at mid-latitudes and a decreased magnitude in the low-latitude region. Similar to EUV, we also use F10.7 to calculate the delay during period 1 and found similar results with slight magnitude differences. The results align with the majority of preceding studies (Ren et al., 2018; Schmölter et al., 2018; Vaishnav, Jacobi, et al., 2021; Vaishnav, Schmölter, et al., 2021). Our findings indicate that utilizing tidal forcing slightly improves the delay estimation and reduces the bias with the observed delay. Consequently, during period 1, the delay using the TIEGCM-HME run aligns more closely with the observational delay (refer to Figure 10). A similar reduction in delay was observed in period 2 for the TIEGCM-HME run compared to the TIEGCM run but increase bias with the observed delay. However, it is important to note that the observed delay is higher in the case of period 2 when compared to period 1.

To assess the performance of TIEGCM and TIEGCM-HME, we calculated the RMSE values between the observed and modeled ionospheric delay. The results indicate that period 1, the RMSE between IGS and TIEGCM estimated delays using EUV is about 4.5 hr, and it decreases to about 4.3 hr with TIEGCM-HME. The RMSE between IGS and TIEGCM estimated delays using F10.7 is about 5 hr, and it decreases to about 4.6 hr with TIEGCM-HME. For low- and mid-latitudes, the RMSE values are about 3.3 hr and about 3.1 hr in the case of TIEGCM and TIEGCM-HME delays using F10.7, while for EUV it was 3 hr for TIEGCM and reduced to 2.70 hr for TIEGCM-HME, respectively. In period 2, the RMSE does not show significant variation. The results indicate a slight improvement when tidal forcing is included, especially during periods of low solar activity.

We have observed variations in ionospheric delay with altitude. At altitudes between 200 and 350 km, the delay ranges from 15 to 25 hr in the TIEGCM run. A difference in delay was noted when using tidal input between approximately 250–340 km. Comparing the TIEGCM run to the TIEGCM-HME run, the ionospheric delay increases in NH low-latitudes by about 1–4 hr during period 1. Additionally, a decrease in delay was observed in low-latitudes SH and mid-latitude NH by about 1–3 hr. Similar delay characteristics were observed during period 2, with differences in magnitude in the TIEGCM run. Comparing the TIEGCM to the TIEGCM-HME run, the delay decreases in low-latitude SH by about 1–8 hr above 260 km. These findings suggest a significant difference in ionospheric delay, primarily attributed to lower atmospheric forcing. Upon reviewing Figure 7, it becomes evident that in the SH low-latitudes, there is a noticeable decrease in the correlation between TIEGCM-HME NmF2 and O/N_2 when compared to the TIEGCM run. The observed changes in delay is consistent with changes in correlation Figure 12. It is worth noting that the lower correlation is associated with an decrease in ionospheric delay.

Previously, Vaishnav, Jacobi, et al. (2021) used the CTIPe model control simulations to showcase the role of transport processes in ionospheric delay. The current investigation, which utilizes more realistic model simulations, strongly affirms these findings and underscores the importance of lower atmospheric forcing in ionospheric delay. This is particularly evident during low solar activity.

The main findings obtained from this study are as follows:

- The model simulation suggests that during periods of low solar activity, the TI parameters are significantly affected by lower atmospheric forcing.
- The change in delay can be attributed to the tidal forcing and its influence on the overall TI system.
- The inclusion of tidal forcing clearly improves the modeled delay and reduces the difference from the observed delay specifically during low solar activity conditions.
- The change in delay may also be subject to multiple factors, such as solar, geomagnetic activity, and transport processes, which may vary depending on the prevailing solar activity.

The ongoing investigation incorporates the use of atmospheric tides based on ICON-MIGHTI data from 94 to 102 km within the latitude range of 10°S–40°N over a 35-day window. More frequent observations would be beneficial for accurately capturing higher-order HME modes, essential for conducting a more detailed investigation of the ionospheric delay.

Conflict of Interest

The authors declare no conflicts of interest relevant to this study.

Data Availability Statement

IGS TEC maps can be downloaded from https://cddis.nasa.gov/archive/gnss/products/ionex/ (NASA, 2024a). GOLD O/N_2 can be downloaded from http://gold.cs.ucf.edu/search/ (NASA, 2024b). Daily Kp indices have been downloaded from https://omniweb.gsfc.nasa.gov/form/dx1.html (NASA, 2024c). The F10.7 index at 1 AU have been obtained from the LISIRD database (LASP, 2024a, https://lasp.colorado.edu/lisird/). The SOHO/SEM EUV flux data have been downloaded from https://lasp.colorado.edu/eve/data_access/eve_data/lasp_soho_sem_data/long/15_sec_avg/ (LASP, 2024b). The TIEGCM simulation data used for this work can be accessed at https://spdf.gsfc.nasa.gov/pub/data/icon/l4/ (NASA, 2024d).

Acknowledgments
The authors thank Dr. Thomas J. Immel and the ICON Science Data Center for providing the ICON-TIEGCM data sets. ICON is supported by NASA's Explorers Program through contracts NNG12FA45C and NNG12FA42I. The study has been supported by Deutsche Forschungsgemeinschaft (DFG) through Grants JA 836/48-1 and SCHM 3761/1-1. Open Access funding enabled and organized by Projekt DEAL.

References

Afraimovich, E. L., Astafyeva, E. I., Oinats, A. V., Yasukevich, Y. V., & Zhivetiev, I. V. (2008). Global electron content: A new conception to track solar activity. *Annales Geophysicae*, *26*(2), 335–344. https://doi.org/10.5194/angeo-26-335-2008

Cai, X., Burns, A. G., Wang, W., Qian, L., Solomon, S. C., Eastes, R. W., et al. (2021). Investigation of a neutral "Tongue" observed by GOLD during the geomagnetic storm on May 11, 2019. *Journal of Geophysical Research: Space Physics*, *126*(6). https://doi.org/10.1029/2020ja028817

Chau, J. L., Goncharenko, L. P., Fejer, B. G., & Liu, H.-L. (2012). Equatorial and low latitude ionospheric effects during sudden stratospheric warming events: Ionospheric effects during SSW events. *Space Science Reviews*, *168*(1–4), 385–417. https://doi.org/10.1007/s11214-011-9797-5

Codrescu, M. V., Negrea, C., Fedrizzi, M., Fuller-Rowell, T. J., Dobin, A., Jakowsky, N., et al. (2012). A real-time run of the coupled thermosphere ionosphere plasmasphere electrodynamics (CTIPe) model. *Space Weather*, *10*(2). https://doi.org/10.1029/2011sw000736

Correira, J., Evans, J. S., Lumpe, J. D., Krywonos, A., Daniell, R., Veibell, V., et al. (2021). Thermospheric composition and solar EUV flux from the global-scale observations of the limb and disk (GOLD) mission. *Journal of Geophysical Research: Space Physics*, *126*(12). https://doi.org/10.1029/2021ja029517

Cullens, C. Y., Immel, T. J., Triplett, C. C., Wu, Y.-J., England, S. L., Forbes, J. M., & Liu, G. (2020). Sensitivity study for ICON tidal analysis. *Progress in Earth and Planetary Science*, *7*, 1–13. https://doi.org/10.1186/s40645-020-00330-6

Eastes, R. W., McClintock, W. E., Burns, A. G., Anderson, D. N., Andersson, L., Aryal, S., et al. (2020). Initial observations by the GOLD mission. *Journal of Geophysical Research: Space Physics*, *125*(7). https://doi.org/10.1029/2020ja027823

Eastes, R. W., McClintock, W. E., Burns, A. G., Anderson, D. N., Andersson, L., Codrescu, M., et al. (2017). The global-scale observations of the limb and disk (GOLD) mission. *Space Science Reviews*, *212*(1–2), 383–408. https://doi.org/10.1007/s11214-017-0392-2

Emery, B., Roble, R. G., Ridley, E. C., Richmond, A. D., Knipp, D. J., Crowley, G., et al. (2012). *Parameterization of the ion convection and the auroral oval in the NCAR thermospheric general circulation models* Tech. rep. National Center for Atmospheric Research. https://doi.org/10.5065/D6N29TXZ

Fang, T.-W., Akmaev, R., Fuller-Rowell, T., Wu, F., Maruyama, N., & Millward, G. (2013). Longitudinal and day-to-day variability in the ionosphere from lower atmosphere tidal forcing. *Geophysical Research Letters*, *40*(11), 2523–2528. https://doi.org/10.1002/grl.50550

Forbes, J. M., Manson, A., Vincent, R., Fraser, G., Vial, F., Wand, R., et al. (1994). Semidiurnal tide in the 80–150 km region: An assimilative data analysis. *Journal of Atmospheric and Terrestrial Physics*, *56*(10), 1237–1249. https://doi.org/10.1016/0021-9169(94)90062-0

Forbes, J. M., Palo, S. E., & Zhang, X. (2000). Variability of the ionosphere. *Journal of Atmospheric and Solar-Terrestrial Physics*, *62*(8), 685–693. https://doi.org/10.1016/s1364-6826(00)00029-8

Forbes, J. M., Roble, R. G., & Fesen, C. G. (1993). Acceleration, heating, and compositional mixing of the thermosphere due to upward propagating tides. *Journal of Geophysical Research*, *98*(A1), 311–321. https://doi.org/10.1029/92JA00442

Forbes, J. M., Zhang, X., Hagan, M. E., England, S. L., Liu, G., & Gasperini, F. (2017). On the specification of upward-propagating tides for ICON science investigations. *Space Science Reviews*, *212*(1–2), 697–713. https://doi.org/10.1007/s11214-017-0401-5

Forbes, J. M., Zhang, X., Maute, A., & Cullens, C. (2024). Responses of the mean thermosphere circulation, O/N_2 ratio and Ne to solar and magnetospheric forcing from above and tidal forcing from below. *Journal of Geophysical Research: Space Physics*, *129*(3), e2024JA032449. https://doi.org/10.1029/2024JA032449

Goncharenko, L., & Zhang, S.-R. (2008). Ionospheric signatures of sudden stratospheric warming: Ion temperature at middle latitude. *Geophysical Research Letters*, *35*(21). https://doi.org/10.1029/2008GL035684

Granger, C. W. (1969). Investigating causal relations by econometric models and cross-spectral methods. *Econometrica: Journal of the Econometric Society*, *37*(3), 424–438. https://doi.org/10.2307/1912791

Jacobi, C., Jakowski, N., Schmidtke, G., & Woods, T. N. (2016). Delayed response of the global total electron content to solar EUV variations. *Advances in Radio Science*, *14*, 175–180. https://doi.org/10.5194/ars-14-175-2016

Jakowski, N., Fichtelmann, B., & Jungstand, A. (1991). Solar activity control of ionospheric and thermospheric processes. *Journal of Atmospheric and Terrestrial Physics*, *53*(11–12), 1125–1130. https://doi.org/10.1016/0021-9169(91)90061-b

Jones, M., Jr., Drob, D. P., Siskind, D. E., McCormack, J. P., Maute, A., McDonald, S. E., & Dymond, K. F. (2018). Evaluating different techniques for constraining lower atmospheric variability in an upper atmosphere general circulation model: A case study during the 2010 sudden stratospheric warming. *Journal of Advances in Modeling Earth Systems*, *10*(12), 3076–3102. https://doi.org/10.1029/2018MS001440

Jones, M., Jr., Forbes, J. M., & Hagan, M. E. (2014). Tidal-induced net transport effects on the oxygen distribution in the thermosphere. *Geophysical Research Letters*, *41*(14), 5272–5279. https://doi.org/10.1002/2014gl060698

Judge, D. L., McMullin, D. R., Ogawa, H. S., Hovestadt, D., Klecker, B., Hilchenbach, M., et al. (1998). First solar EUV irradiances obtained from SOHO by the SEM. *Solar Physics*, *177*(1/2), 161–173. https://doi.org/10.1023/a:1004929011427

Kazimirovsky, E. S., & Kokourov, V. D. (1991). The tropospheric and stratospheric effects in the ionosphere. *Journal of Geomagnetism and Geoelectricity*, *43*(1), 551–562. https://doi.org/10.5636/jgg.43.Supplement1_551

Knížová, P. K., Laštovička, J., Kouba, D., Mošna, Z., Podolská, K., Potužníková, K., et al. (2021). Ionosphere influenced from lower-lying atmospheric regions. *Frontiers in Astronomy and Space Sciences*, *8*. https://doi.org/10.3389/fspas.2021.651445

Kutiev, I., Tsagouri, I., Perrone, L., Pancheva, D., Mukhtarov, P., Mikhailov, A., et al. (2013). Solar activity impact on the Earth's upper atmosphere. *Journal of Space Weather and Space Climate*, *3*, A06. https://doi.org/10.1051/swsc/2013028

LASP. (2024a). LASP interactive solar irradiance data center [Dataset]. *University of Colorado*. Retrieved from https://lasp.colorado.edu/lisird/

LASP. (2024b). SOHO/SEM flux [Dataset]. Retrieved from https://lasp.colorado.edu/eve/data_access/eve_data/lasp_soho_sem_data/long/15_sec_avg/

Liu, H.-L. (2016). Variability and predictability of the space environment as related to lower atmosphere forcing. *Space Weather*, *14*(9), 634–658. https://doi.org/10.1002/2016SW001450

Liu, H.-L., Wang, W., Richmond, A., & Roble, R. (2010). Ionospheric variability due to planetary waves and tides for solar minimum conditions. *Journal of Geophysical Research*, *115*(A6). https://doi.org/10.1029/2009ja015188

Liu, H.-L., Yudin, V., & Roble, R. (2013). Day-to-day ionospheric variability due to lower atmosphere perturbations. *Geophysical Research Letters*, *40*(4), 665–670. https://doi.org/10.1002/grl.50125

Maute, A. (2017). Thermosphere-ionosphere-electrodynamics general circulation model for the ionospheric connection explorer: TIEGCM-ICON. *Space Science Reviews*, *212*(1–2), 523–551. https://doi.org/10.1007/s11214-017-0330-3

Maute, A., Forbes, J. M., Cullens, C. Y., & Immel, T. J. (2023). Delineating the effect of upward propagating migrating solar tides with the TIEGCM-ICON. *Frontiers in Astronomy and Space Sciences*, *10*, 1147571. https://doi.org/10.3389/fspas.2023.1147571

Min, K., Park, J., Kim, H., Kim, V., Kil, H., Lee, J., et al. (2009). The 27-day modulation of the low-latitude ionosphere during a solar maximum. *Journal of Geophysical Research*, *114*(4), 1–8. https://doi.org/10.1029/2008JA013881

NASA. (2024a). GNSS atmospheric products [Dataset]. Retrieved from https://cddis.nasa.gov/archive/gnss/products/ionex/

NASA. (2024b). GOLD science data products [Dataset]. Retrieved from http://gold.cs.ucf.edu/search/

NASA. (2024c). Omniweb Plus database [Dataset]. Retrieved from http://omniweb.gsfc.nasa.gov/

NASA. (2024d). TIEGCM simulations [Dataset]. Retrieved from https://spdf.gsfc.nasa.gov/pub/data/icon/l4/

Noll, C. E. (2010). The crustal dynamics data information system: A resource to support scientific analysis using space geodesy. *Advances in Space Research*, *45*(12), 1421–1440. https://doi.org/10.1016/j.asr.2010.01.018

Oberheide, J., Forbes, J., Zhang, X., & Bruinsma, S. (2011). Climatology of upward propagating diurnal and semidiurnal tides in the thermosphere. *Journal of Geophysical Research*, *116*(A11). https://doi.org/10.1029/2011JA016784

Oberheide, J., Shiokawa, K., Gurubaran, S., Ward, W. E., Fujiwara, H., Kosch, M. J., et al. (2015). The geospace response to variable inputs from the lower atmosphere: A review of the progress made by task group 4 of CAWSES-II. *Progress in Earth and Planetary Science*, *2*, 1–31. https://doi.org/10.1186/s40645-014-0031-4

Pedatella, N., Fang, T.-W., Jin, H., Sassi, F., Schmidt, H., Chau, J., et al. (2016). Multimodel comparison of the ionosphere variability during the 2009 sudden stratosphere warming. *Journal of Geophysical Research: Space Physics*, *121*(7), 7204–7225. https://doi.org/10.1002/2016JA022859

Qian, L., Burns, A. G., Emery, B. A., Foster, B., Lu, G., Maute, A., et al. (2014). The NCAR TIE-GCM: A community model of the coupled thermosphere/ionosphere system. In *Modeling the ionosphere–thermosphere system* (pp. 73–83). https://doi.org/10.1002/9781118704417.ch7

Qian, L., Gan, Q., Wang, W., Cai, X., Eastes, R., & Yue, J. (2022). Seasonal variation of thermospheric composition observed by NASA GOLD. *Journal of Geophysical Research: Space Physics*, *127*(6). https://doi.org/10.1029/2022ja030496

Qian, L., Solomon, S. C., & Kane, T. J. (2009). Seasonal variation of thermospheric density and composition. *Journal of Geophysical Research*, *114*(A1). https://doi.org/10.1029/2008ja013643

Rees, D., & Fuller-Rowell, T. (1988). Understanding the transport of atomic oxygen within the thermosphere, using a numerical global thermospheric model. *Planetary and Space Science*, *36*(9), 935–948. https://doi.org/10.1016/0032-0633(88)90101-8

Ren, D., Lei, J., Wang, W., Burns, A., Luan, X., & Dou, X. (2018). Does the peak response of the ionospheric F2 region plasma lag the peak of 27-day solar flux variation by multiple days? *Journal of Geophysical Research: Space Physics*, *123*(9), 7906–7916. https://doi.org/10.1029/2018ja025835

Ren, D., Lei, J., Wang, W., Burns, A., Luan, X., & Dou, X. (2019). A simulation study on the time delay of daytime thermospheric temperature response to the 27-day solar EUV flux variation. *Journal of Geophysical Research: Space Physics*, *124*(11), 9184–9193. https://doi.org/10.1029/2019ja027000

Ren, D., Lei, J., Wang, W., Burns, A., Luan, X., & Dou, X. (2020). Different peak response time of daytime thermospheric neutral species to the 27-day solar EUV flux variations. *Journal of Geophysical Research: Space Physics*, *125*(7). https://doi.org/10.1029/2020ja027840

Richards, P. G., Fennelly, J. A., & Torr, D. G. (1994). EUVAC: A solar EUV flux model for aeronomic calculations. *Journal of Geophysical Research*, *99*(A5), 8981–8992. https://doi.org/10.1029/94ja00518

Richmond, A. D., & Maute, A. (2014). Ionospheric electrodynamics modeling. In *Modeling the ionosphere–thermosphere system* (pp. 57–71). https://doi.org/10.1002/9781118704417.ch6

Richmond, A. D., Ridley, E. C., & Roble, R. G. (1992). A thermosphere/ionosphere general circulation model with coupled electrodynamics. *Geophysical Research Letters*, *19*(6), 601–604. https://doi.org/10.1029/92gl00401

Rishbeth, H., & Mendillo, M. (2001). Patterns of F2-layer variability. *Journal of Atmospheric and Solar-Terrestrial Physics*, *63*(15), 1661–1680. https://doi.org/10.1016/s1364-6826(01)00036-0

Roble, R., & Ridley, E. (1987). An auroral model for the NCAR thermospheric general circulation model (TGCM). *Annales Geophysicae*, *5*, 369–382.

Schmölter, E., Berdermann, J., & Codrescu, M. (2021). The delayed ionospheric response to the 27-day solar rotation period analyzed with GOLD and IGS TEC data. *Journal of Geophysical Research: Space Physics*, *126*(2). https://doi.org/10.1029/2020ja028861

Schmölter, E., Berdermann, J., Jakowski, N., & Jacobi, C. (2020). Spatial and seasonal effects on the delayed ionospheric response to solar EUV changes. *Annales Geophysicae*, *38*(1), 149–162. https://doi.org/10.5194/angeo-38-149-2020

Schmölter, E., Berdermann, J., Jakowski, N., Jacobi, C., & Vaishnav, R. (2018). Delayed response of the ionosphere to solar EUV variability. *Advances in Radio Science*, *16*, 149–155. https://doi.org/10.5194/ars-16-149-2018

Schmölter, E., Dühnen, H., Berdermann, J., Vaishnav, R., & Jacobi, C. (2024). Spatial features of the delayed ionospheric response during low and high solar activity. *Journal of Geophysical Research: Space Physics*, *129*(5), e2024JA032672. https://doi.org/10.1029/2024JA032672

Schmölter, E., Heymann, F., Savigny, C., & Berdermann, J. (2022). The height-dependent delayed ionospheric response to solar EUV. *Journal of Geophysical Research: Space Physics*, *127*(3). https://doi.org/10.1029/2021ja030118

Schmölter, E., & von Savigny, C. (2022). Solar activity driven 27-day signatures in ionospheric electron and molecular oxygen densities. *Journal of Geophysical Research: Space Physics*, *127*(9). https://doi.org/10.1029/2022ja030671

Shojaie, A., & Fox, E. B. (2022). Granger causality: A review and recent advances. *Annual Review of Statistics and Its Application*, *9*(1), 289–319. https://doi.org/10.1146/annurev-statistics-040120-010930

Siskind, D., Drob, D., Dymond, K., & McCormack, J. (2014). Simulations of the effects of vertical transport on the thermosphere and ionosphere using two coupled models. *Journal of Geophysical Research: Space Physics*, *119*(2), 1172–1185. https://doi.org/10.1002/2013JA019116

Vaishnav, R., Jacobi, C., & Berdermann, J. (2019). Long-term trends in the ionospheric response to solar extreme-ultraviolet variations. *Annales Geophysicae*, *37*(6), 1141–1159. https://doi.org/10.5194/angeo-37-1141-2019

Vaishnav, R., Jacobi, C., Berdermann, J., Codrescu, M., & Schmölter, E. (2021). Role of eddy diffusion in the delayed ionospheric response to solar flux changes. *Annales Geophysicae*, *39*(4), 641–655. https://doi.org/10.5194/angeo-39-641-2021

Vaishnav, R., Jacobi, C., Berdermann, J., Schmölter, E., & Codrescu, M. (2018). Ionospheric response to solar EUV variations: Preliminary results. *Advances in Radio Science*, *16*, 157–165. https://doi.org/10.5194/ars-16-157-2018

Vaishnav, R., Jacobi, C., Berdermann, J., Schmölter, E., & Codrescu, M. (2022). Delayed ionospheric response to solar extreme ultraviolet radiation variations: A modeling approach. *Advances in Space Research*, *69*(6), 2460–2476. https://doi.org/10.1016/j.asr.2021.12.041

Vaishnav, R., Jacobi, C., Berdermann, J., Schmölter, E., Dühnen, H., & Codrescu, M. (2024). Ionospheric response to solar EUV radiation variations using GOLD observations and the CTIPe model. *Journal of Geophysical Research: Space Physics*, *129*(1), e2022JA030887. https://doi.org/10.1029/2022JA030887

Vaishnav, R., Schmölter, E., Jacobi, C., Berdermann, J., & Codrescu, M. (2021). Ionospheric response to solar extreme ultraviolet radiation variations: Comparison based on CTIPe model simulations and satellite measurements. *Annales Geophysicae*, *39*(2), 341–355. https://doi.org/10.5194/angeo-39-341-2021

Weimer, D. (2005). Improved ionospheric electrodynamic models and application to calculating Joule heating rates. *Journal of Geophysical Research*, *110*(A5). https://doi.org/10.1029/2004JA010884

Yamazaki, Y., & Richmond, A. D. (2013). A theory of ionospheric response to upward-propagating tides: Electrodynamic effects and tidal mixing effects. *Journal of Geophysical Research: Space Physics*, *118*(9), 5891–5905. https://doi.org/10.1002/jgra.50487

Yiğit, E., & Medvedev, A. S. (2015). Internal wave coupling processes in Earth's atmosphere. *Advances in Space Research*, *55*(4), 983–1003. https://doi.org/10.1016/j.asr.2014.11.020

Zhang, Y., & Paxton, L. J. (2011). Long-term variation in the thermosphere: TIMED/GUVI observations. *Journal of Geophysical Research*, *116*(A2). https://doi.org/10.1029/2010ja016337

Zhou, X., Liu, H.-L., Lu, X., Zhang, R., Maute, A., Wu, H., et al. (2020). Quiet-time day-to-day variability of equatorial vertical E × B drift from atmosphere perturbations at dawn. *Journal of Geophysical Research: Space Physics*, *125*(4), e2020JA027824. https://doi.org/10.1029/2020JA027824

Zhou, X., Yue, X., Liu, H.-L., Lu, X., Wu, H., Zhao, X., & He, J. (2021). A comparative study of ionospheric day-to-day variability over Wuhan based on ionosonde measurements and model simulations. *Journal of Geophysical Research: Space Physics*, *126*(3), e2020JA028589. https://doi.org/10.1029/2020JA028589